

High Resolution Carrier Frequency Offset Estimation in Time-Reversal Wideband Communications

Chen Chen¹, Yan Chen, *Senior Member, IEEE*, Yi Han, Hung-Quoc Lai, *Member, IEEE*,
and K. J. Ray Liu, *Fellow, IEEE*

Abstract—Time-reversal (TR) wideband communication systems enjoy the spatial-temporal focusing effect in a rich-scattering environment. However, the performance degrades in the presence of carrier frequency offset (CFO). The impact of CFO can be mitigated by compensating the estimated CFO values obtained using CFO estimators. Yet, CFO estimators in literature cannot work well in wideband TR systems due to the fact that the normalized CFO values are very small and thus cannot be estimated accurately using conventional schemes. To address this issue, we propose four CFO estimators which are capable of accurate CFO estimations for wideband TR systems. The theoretical performances of the proposed estimators are analyzed. Additionally, realizing that phase wrapping might introduce severe bias into CFO estimations, we present the conditions on the system parameters so that phase wrapping can be avoided. Extensive simulations and experimental results demonstrate the superiority of the proposed methods.

Index Terms—Time-reversal wideband communication, carrier frequency offset, estimation, phase wrapping, time-reversal focusing effect.

I. INTRODUCTION

IN WIRELESS communication, carrier frequency offset (CFO) occurs when the local oscillator for downconversion at the receiver fails to fully synchronize with the local oscillator for upconversion at the transmitter in terms of the center frequency [1]. It degrades the wireless communication systems by introducing a linear phase rotation, destroying the orthogonality between different users, and undermining

the accuracy of the initial cell search in direct-sequence code division multiple access (DS-CDMA) systems [2], [3]. In the orthogonal frequency-division modulation (OFDM) multi-carrier systems, CFO introduces attenuation onto useful signals and harms the orthogonality among subcarriers [1], [4].

Many efforts have been made to address the CFO issue. Uolkosold *et al.* propose a non-linear least-square (NLS) CFO estimator for flat-fading channels [5]. The estimator searches for the spectral maxima after performing fast Fourier transform (FFT). Keller and Hanzo devise an estimator based on the cyclic prefix which leverages the delay and correlation algorithm for the calculation of a timing metric in OFDM systems [6], and it searches for the maximum peak of the timing metric for symbol timing and CFO estimation. An improved timing metric is studied by Beek *et al.* in [7] with the log-likelihood function for the received signal parameterized by CFO and symbol timing offset derived. Maximizing the log-likelihood function leads to a joint estimation of the symbol timing and CFO. Different from [7], Schmidl and Cox leverage the training sequence (TS) with two identical halves before the data frames [8]. Within a sliding window, the receiver computes the averaged and normalized auto-correlation function. Then, a joint estimation of timing offset and CFO estimation is formulated by locating the peak in the timing metric. To improve the performance, two novel training sequences are presented by Minn *et al.* [9] and Kim *et al.* [10].

Recently, time-reversal (TR) wideband communication is attracting more and more attention since it can fully harness the energy of multipath components in the rich-scattering environment for wireless communication [11]. It is an ideal paradigm for low-complexity, low energy consumption green wireless communication [12]. In virtue of its asymmetric architecture, only one-tap detection is required at the TR receiver [13]. As a result, the complexity of the TR receiver is reduced significantly in comparison with the OFDM receivers [14] and single-carrier receivers using frequency-domain equalizer (FDE) [15].

However, like other wireless communication systems, TR systems suffer from CFO. As a wideband system, TR systems impose a more stringent requirement on the accuracy of CFO estimation since within the same time slot, more symbols would be affected by the CFO in comparison with narrowband systems. Yet, to the best of our knowledge, there is no existing

Manuscript received March 21, 2017; revised July 24, 2017 and September 5, 2017; accepted September 5, 2017. Date of publication September 13, 2017; date of current version May 15, 2018. The associate editor coordinating the review of this paper and approving it for publication was Y. Wu. (*Corresponding author: Chen Chen.*)

C. Chen is with Origin Wireless Inc., Greenbelt, MD 20770 USA, and also with the Department of Electrical and Computer Engineering, University of Maryland, College Park, MD 20742 USA (e-mail: cc8834@umd.edu).

Y. Chen was with Origin Wireless Inc., Greenbelt, MD 20770 USA. He is now with the School of Electronic Engineering, University of Electronic Science and Technology of China, Chengdu 610051, China (e-mail: eecyan@uestc.edu.cn).

Y. Han and H.-Q. Lai are with Origin Wireless Inc., Greenbelt, MD 20770 USA (e-mail: yi.han@originwireless.net; quoc.lai@originwireless.net).

K. J. R. Liu is with Origin Wireless Inc., Greenbelt, MD 20770 USA, and also with the Department of Electrical and Computer Engineering, University of Maryland, College Park, MD 20742 USA (e-mail: kjrlu@umd.edu).

Color versions of one or more of the figures in this paper are available online at <http://ieeexplore.ieee.org>.

Digital Object Identifier 10.1109/TCOMM.2017.2751609

work in the literature studying the effect of CFO in TR communication systems, nor proposing methods to address it. On the other hand, existing CFO estimation schemes cannot work well in TR systems due to the following reasons: (i) the high sampling rate in TR wideband systems [16] makes the normalized CFO very small. Thus, a long training sequence is needed in the training-based schemes to estimate the tiny CFO accurately, incurring significant training overhead. (ii) Since the cyclic prefix blocks associated with different data blocks differ from each other, schemes leveraging cyclic prefix are unable to reuse the same cyclic prefix block. As we show in this paper, schemes with reusing outperform those without reusing. (iii) Most CFO estimators neglect the issue of phase wrapping, which introduces bias into CFO estimations [17].

In this paper, we investigate the impact of CFO on TR wideband communication systems and propose methods to counteract CFO. Identical pilot blocks are inserted into data frames. With the assistance of these pilot blocks, we propose four different CFO estimation methods, i.e., angle-of-mean/mean-of-angle with/without reusing. The main idea is: the phase of the average correlation between two pilot blocks is linear in the CFO. Theoretical analysis on the bias and mean-square-error (MSE) of different methods is presented as well. Additionally, we study the impact of phase wrapping on the performances and discuss the way to avoid it. The effect of CFO on the TR focusing gain is also analyzed. Extensive simulation and experimental results demonstrate the superior performance of the proposed methods.

The rest of this paper is organized as follows. We present a brief background review on the TR technique in Section II. Then, we introduce the system model in Section III and propose four CFO estimators in Section IV. Theoretical analyses are conducted in Section V. Simulation and experimental results are presented in Section VI and VII, respectively. Finally, we draw conclusions in Section VIII.

Notations: x denotes a scalar, and \mathbf{x} denotes a vector. \mathbb{Z}^+ denotes the set of positive integers. $\mathcal{CN}(\mu, \sigma^2)$ denotes the complex Gaussian distribution with mean μ and variance σ^2 . $\Re[X]$ and $\Im[X]$ are the real and imaginary part of a complex argument X . $\text{atan}[X]$ is the arctangent of argument X . $\angle[X] = \text{atan}\left[\frac{\Im[X]}{\Re[X]}\right]$ is the angle of the complex argument X . For a random variable X , $\mathbb{E}[X]$ and $\text{Var}[X]$ stand for the expectation and variance of X . For an estimator \hat{X} , $\text{Bias}[\hat{X}]$ and $\text{MSE}[\hat{X}]$ denote the bias and mean squared error (MSE) for the estimation. $*$ stands for the linear convolution, and X^* stands for the conjugate of a complex argument X . $\|\mathbf{x}\|_2$ stands for the L_2 norm of vector \mathbf{x} .

II. BRIEF HISTORY OF TIME REVERSAL

Computational time-reversal is a signal processing technique that could focus the energy of the wave onto the source location from where the wave is emitted [18]. The history of the computational TR dates back to 1950's when Bogert uses TR to correct delay distortion in a slow-speed picture transmission system [19]. Later, it is shown by Amoroso that the TR waveform is the optimal solution to a constrained optimization problem in digital communications [20].

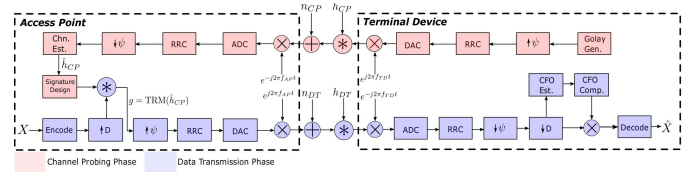


Fig. 1. Architecture of the time-reversal communication system.

An important property of TR is the spatial-temporal focusing effect: the energy of signal waves is concentrated at a specific location in the space and at a specific time instance. This effect is verified experimentally using ultrasonic and acoustics waves [21], [22], and later with electromagnetic waves [12].

Thanks to the focusing effect, TR is widely used in a variety of applications. In [23], Devaney utilized TR-MUSIC algorithm to resolve targets within a certain area, known as TR imaging. The performance of TR-MUSIC is studied in [24] and its stability is analyzed in [25]. Moura and Jin adopted TR in a single antenna system and later an antenna array for target detection in highly cluttered environment [26], [27]. Moreover, TR is a promising candidate in future 5G communication systems, since it could collectively address the major challenges in indoor wireless communications, thanks to its massive multipath effect, high capacity, and scalability [28]. In [13], Han *et al.* presented a TR-based multi-user multiple access wireless communication system.

Additionally, TR is a promising paradigm for green internet-of-things (IoT) by extending the battery life, accommodating low-cost and heterogeneous terminals, and providing physical layer security [11], [29]. Applications of TR in IoT include centimeter-level indoor localization [30], [31], human recognition [32], event detection [33], speed estimation [34], and monitoring of vital signs [35].

III. SYSTEM MODEL

The architecture of the TR wireless communication system is shown in Fig. 1. One cycle of TR transmission consists of a channel probing (CP) phase and a data transmission (DT) phase. In the CP phase, the terminal device (TD) sends a CP signal to the access point (AP) to facilitate channel impulse response (CIR) estimation. In this work, we consider the Golay sequence [36] as the CP signal. Then, AP generates a signature g based on the estimated CIR. In the DT phase, AP convolves the encoded signal with the signature g . The transmitted signal convolves with the channel naturally, which is mathematically equivalent to the matched filtering. TD estimates and mitigates CFO, and decodes the signal using a Viterbi decoder.

TR wireless communication utilizes the channel reciprocity and that the channel remains static during the TR transmission. Both features are verified experimentally in [12].

Thanks to the asymmetric structure, the complexity of TDs can be driven down dramatically since both channel estimator and equalizer are not required at TDs. Nevertheless, CFO inevitably disturbs the performance of TR systems. It affects both the CP phase and the DT phase in two different ways: CFO gives rise to phase distortion into the signature g at the access point in the CP phase, while it leads to a time-varying phase rotation at the terminal device in the DT phase.

Both effects are described in details in the subsequent part of this section.

A. Signal Model in Channel Probing Phase

In the CP phase, TD constructs and sends a Golay sequence composed with -1 and 1 with a length of L_{GS} to facilitate accurate channel estimation, denoted as $\mathbf{G} = \{G[k]\}_{k=0,1,\dots,L_{GS}-1}$ generated by the low-complexity scheme proposed in [37]. Denote its scaled and time-reversed version given as $\tilde{\mathbf{G}} = \{\tilde{G}[k]\}_{k=0,1,\dots,L_{GS}-1}$ with $\tilde{G}[k] = \frac{G[L_{GS}-1-k]}{L_{GS}}$, $k = 0, 1, \dots, L_{GS}-1$, the cross correlation between \mathbf{G} and $\tilde{\mathbf{G}}$ is defined as

$$\begin{aligned} J[n] &= \sum_{k=\max(0,n+1-L_{GS})}^{\min(L_{GS}-1,n)} G[k]\tilde{G}[n-k] \\ &= \frac{1}{L_{GS}} \sum_{k=\max(0,n+1-L_{GS})}^{\min(L_{GS}-1,n)} G[k]G[L_{GS}-1-n+k], \\ n &= 0, 1, \dots, 2L_{GS}-2 \end{aligned} \quad (1)$$

which equals 1 at $n = L_{GS}-1$ and much smaller when $n > 0$.

On reception of the transmitted Golay sequence from TD, AP performs a decimation with a factor of ψ . The k -th received signal is denoted as $Y_{CP}[k]$ which takes the form below:

$$Y_{CP}[k] = (G * h_{CP})[k]e^{j2\pi\Delta f T_s \psi k} + n_{CP}[k], \quad (2)$$

where $\{h_{CP}[\ell]\}_{\ell=0,1,\dots,L-1}$ is the L -tap CIR between the AP and the TD in the CP phase.¹ Assume that the CIR reciprocity to hold and that the CIR remains static, we could rewrite $h_{CP}[\ell]$ as $h[\ell]$. $\Delta f = f_{AP} - f_{TD}$ is the CFO, i.e., the difference between the local oscillator frequencies at the TD and that at the AP, $n_{CP}[k] \sim \mathcal{CN}(0, \sigma_{CP}^2)$ is the channel noise in the CP phase, T_s is the sampling interval before decimation, and $T_b = \psi T_s$ the baseband sampling interval after decimation.

The CIR can be estimated by convolving the received signal in (2) with $\tilde{\mathbf{G}}$. The estimated CIR can be expressed by

$$\begin{aligned} \hat{h}[\ell] &= (\tilde{\mathbf{G}} * Y_{CP})[\ell + L_{GS} - 1] \\ &= \sum_{\ell'=0}^{L-1} h[\ell'] \sum_{m=0}^{L_{GS}-1} \tilde{G}[m]G[\ell + L_{GS} - 1 - \ell' - m] \\ &\quad \times e^{j2\pi\Delta f T_s \psi (\ell + L_{GS} - 1 - m)} + n'[\ell + L_{GS} - 1], \end{aligned} \quad (3)$$

where $n'[k] = (\tilde{\mathbf{G}} * n_{CP})[k]$. Since $\tilde{\mathbf{G}}$ contains a scaling factor of $1/L_{GS}$, $n'[k]$ can be regarded as a summation of many zero mean complex Gaussian noises scaled by a factor of $1/L_{GS}$. When L_{GS} is sufficiently large, $n'[k]$ can be ignored. Meanwhile, $\Delta f T_s$ is very small in wideband TR systems, $e^{j2\pi\Delta f T_s \psi (\ell + L_{GS} - 1 - m)}$ can be approximated as $e^{j2\pi\Delta f T_s \psi (\ell + L_{GS} - 1)}$ for all m . As $\sum_{m=0}^{L_{GS}-1} \tilde{G}[m]G[\ell + L_{GS} - 1 - \ell' - m]$ has a strong peak when $\ell = \ell'$ due to (1), (3) can be approximated as

$$\hat{h}[\ell] \approx h[\ell]e^{j\Delta\omega\psi\ell}e^{j\theta} \quad (4)$$

where $\Delta\omega = 2\pi\Delta f T_s$ is the normalized CFO (NCFO), and $\theta = 2\pi\Delta f T_s \psi (L_{GS} - 1)$ is the common phase error (CPE).

¹In the presence of pulse shaping filters, the CIR can be considered as the effective channel expressed as the linear convolution between the physical channel and the pulse shaping filters.

B. Signal Model in Data Transmission Phase

In the DT phase, the received baseband signal after decimation ψ and back-off D is given by [12]

$$Y[k] = S[k]e^{-j\Delta\omega D\psi k}e^{-j\theta} + n_{DT}[k], \quad (5)$$

where

$$\begin{aligned} S[k] &= \underbrace{(h * g)[L-1]X\left[k - \frac{L-1}{D}\right]}_{S_1[k]} \\ &\quad + \underbrace{\sum_{l=0, l \neq (L-1)/D}^{(2L-2)/D} (h * g)[Dl]X[k-l]}_{S_2[k]}. \end{aligned} \quad (6)$$

In (6), $X[k]$ is the k -th transmitted symbol with $X[k] = 0$, $\forall k < 0$, and D is the back-off rate. As shown in [12], the inter-symbol-interference reduces as D increases. $n_{DT}[k]$ is the zero-mean complex Gaussian noise with variance σ^2 , $S_1[k]$ is the useful part which carries the transmitted symbol, and $S_2[k]$ is the inter-symbol-interference (ISI). $g[k]$ the signature given by

$$g[k] = \frac{\hat{h}^*[L-1-k]}{\sqrt{\sum_{\ell=0}^{L-1} |\hat{h}[\ell]|^2}} = \frac{h^*[L-1-k]e^{-j\Delta\omega(L-1-k)\psi}}{\sqrt{\sum_{\ell=0}^{L-1} |h[\ell]|^2}}, \quad (7)$$

where the noise in channel estimation is neglected when L_{GS} is sufficiently large.

Substituting $g[k]$ into $S[k]$ yields

$$S[k] = \beta(\Delta\omega)X[k-L']e^{-j\theta} + \eta[k], \quad (8)$$

where $L' = \frac{L-1}{D}$ and is assumed to be a positive integer.² $\eta[k]$ is the ISI given by

$$\begin{aligned} \eta[k] &= \sum_{\ell=0, \ell \neq L'}^{(2L-2)/D} \sum_{\ell'=0}^{L-1} \frac{1}{\sqrt{\sum_{\ell=0}^{L-1} |h[\ell]|^2}} h[\ell'] \\ &\quad \times h^*[L-1-D\ell+\ell']e^{-j\Delta\omega\psi(L-1-D\ell+\ell')}e^{-j\theta}X[k-\ell], \end{aligned} \quad (9)$$

and

$$\beta(\Delta\omega) = \frac{\sum_{\ell=0}^{L-1} |h[\ell]|^2 e^{-j\Delta\omega\psi\ell}}{\sqrt{\sum_{\ell=0}^{L-1} |h[\ell]|^2}} = |\beta(\Delta\omega)|e^{j\angle[\beta(\Delta\omega)]} \quad (10)$$

is the complex scaling factor by using the signature $g[k]$ in (7) under $\Delta\omega$. Its amplitude $|\beta(\Delta\omega)|$ is termed as the *TR focusing gain*. When $\Delta\omega = 0$, the TR focusing gain attains its maximum as [12]

$$|\beta(0)| = \beta(0) = \sqrt{\sum_{\ell=0}^{L-1} |h[\ell]|^2}, \quad \angle[\beta(0)] = 0 \quad (11)$$

indicating that TR technique fully harnesses the rich-scattering environment by combining multipaths components coherently.

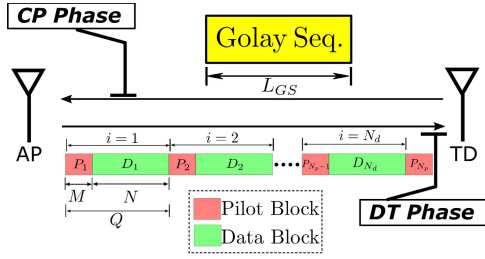


Fig. 2. Frame structure of the TR system in the channel probing phase and data transmission phase.

IV. CARRIER FREQUENCY OFFSET ESTIMATION

Fig. 2 demonstrates the frame structures in both the CP and DT phases. According to the simulation results as shown in Fig. 4(b) in Section VI, $\Delta\omega$ has very limited effect on the signature $g[k]$ in (7) when $\Delta\omega = 8 \times 10^{-5}$. Therefore, CFO estimation is not compulsory in the CP phase for typical CFO values on the order of 10^{-5} . Meanwhile, to facilitate CFO estimation in the DT phase, we insert identical pilot blocks $P_1, P_2, \dots, P_{N_p-1}$ into data blocks D_1, D_2, \dots, D_{N_d} and we append an additional pilot block P_{N_p} behind the last data block D_{N_d} . Here, N_p and N_d represent the total number of pilot and data blocks, where $N_p = N_d + 1$. The length for each pilot block is M and that of each data block is N . The length of one transmission block is thus $Q = M + N$. The block index is denoted as i .

Given the frame structure in Fig. 2, $\Delta\omega$ can be estimated by first calculating the auto-correlation $\Phi_{n_1, n_2}[k]$ using symbols inside the n_1 -th and n_2 -th pilot blocks, expressed as

$$\begin{aligned} \Phi_{n_1, n_2}[k] &= Y[k + n_1 Q + L'] Y^*[k + n_2 Q + L'] \\ &= |S[k]|^2 e^{j\Delta\omega D\psi(n_2 - n_1)Q} \\ &\quad + n[k + L' + n_1 Q] S^*[k + L' + n_2 Q] e^{j(\Delta\omega D\psi(k + L' + n_2 Q) + \theta)} \\ &\quad + n^*[k + L' + n_2 Q] S[k + L' + n_1 Q] e^{-j(\Delta\omega D\psi(k + L' + n_1 Q) + \theta)} \\ &\quad + n[k + L' + n_1 Q] n^*[k + L' + n_2 Q], \end{aligned} \quad (12)$$

with $Y[k]$ given in (5) and $n_{DT}[k]$ is written as $n[k]$ for convenience. Thus, $\Delta\omega$ can be estimated as

$$\widehat{\Delta\omega} = \frac{\angle \left[\frac{1}{M} \Phi_{i, i+1}[k] \right]}{Q D \psi}, \quad (13)$$

where the pilot block index i takes value in $\{0, 1, \dots, N_p - 2\}$.

Inspired by (13), we propose four estimators:

$$\widehat{\Delta\omega} = \begin{cases} \frac{\angle \left[\frac{2}{MN_p} \sum_{i=0}^{N_p/2-1} \sum_{k=0}^{M-1} \Phi_{2i, 2i+1}[k] \right]}{Q\psi D}, & \text{AOM-NR} \\ \frac{2 \sum_{i=1}^{N_p/2} \angle \left[\frac{1}{M} \sum_{k=0}^{M-1} \Phi_{2i, 2i+1}[k] \right]}{N_p Q \psi D}, & \text{MOA-NR} \\ \frac{\angle \left[\frac{1}{M(N_p-1)} \sum_{i=0}^{N_p-2} \sum_{k=0}^{M-1} \Phi_{i, i+1}[k] \right]}{Q\psi D}, & \text{AOM-R} \\ \frac{\sum_{i=0}^{N_p-2} \angle \left[\frac{1}{M} \sum_{k=0}^{M-1} \Phi_{i, i+1}[k] \right]}{(N_p - 1) Q \psi D}, & \text{MOA-R} \end{cases} \quad (14)$$

²In practice, L' is estimated from short preambles in the TR DT phase, which is out of the scope of this paper.

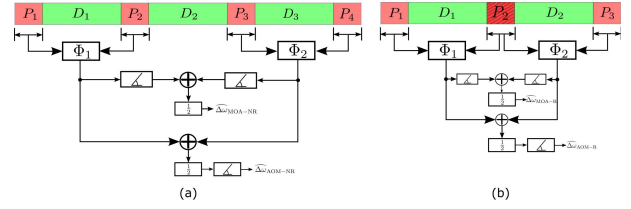


Fig. 3. Architecture of the proposed methods. (a) Schemes without reusing pilot block, $N_d = 3$, $N_p = 4$. (b) Schemes reusing pilot block P_2 , $N'_d = 2$, $N'_p = 3$.

where **AOM** stands for Angle-of-Mean, **MOA** for Mean-of-Angle, **R** for reusing, and **NR** for non-reusing. N_p is the number of pilot blocks for the non-reusing schemes, while N'_p is the counterpart for the reusing schemes.

The four variants mainly differ in two aspects: (i) the operational sequences of mean and taking angle (ii) whether or not the same pilot blocks are used. These two aspects are analyzed as follows:

- The MOA schemes are more complicated than the AOM counterparts. This is because that only one angle operator (\angle) is needed in the AOM, while MOA uses $N_p/2$ angle operators. However, MOA schemes are more suitable for tracking time-varying CFO values: for each pair of pilot blocks, MOA scheme generates one CFO estimation which can be used to compensate the data block immediately, while AOM scheme calculates the CFO after receiving multiple pairs of pilot blocks.
- The reusing schemes reuse the same pilot blocks to enhance the estimation performance in comparison with the non-reusing methods, which is shown later in this section. However, reusing the same pilot block requires an extra buffer dedicated to store the pilot block and the overhead can be costly when the pilot block size is large.

We illustrate the proposed schemes in Fig. 3. In the non-reusing schemes, we calculate Φ_1 from P_1 and P_2 , and Φ_2 from P_3 and P_4 , while in the reusing schemes, we reuse the same pilot block P_2 to calculate Φ_1 and Φ_2 .

Remark 1: The proposed estimators resemble the maximum likelihood estimator (MLE) on CFO given multiple identical preamble blocks proposed by Cheng and Chou [38]. More specifically, for a total of $N'_p = B + 1$ pilot blocks, the MLE takes the form below:

$$\widehat{\Delta\omega}_{\text{MLE}} = \frac{1}{Q\psi D} \sum_{m=1}^B \frac{1}{m} \angle \left[\sum_{k=0}^{M-1} \sum_{p=m}^B \Phi_{p-m, p}[k] \right]. \quad (15)$$

The Cramér-Rao lower bound (CRLB) for the CFO estimation is derived as well in [38] for multiple identical preamble blocks. Under the notations of this paper, the CRLB is given as

$$\text{CRLB}[\Delta\omega] = \frac{6\sigma^2(\sigma^2 + B + 1)}{MQ^2\psi^2 D^2 (B + 1)^2 [(B + 1)^2 - 1]}. \quad (16)$$

The difference between the MLE in (15) and the proposed estimators are listed as follows:

- The MLE estimator in (15) considers all possible separations between pilot blocks, i.e., $Q, 2Q, 3Q, \dots, BQ$ for $B + 1$ pilot blocks, indicated by $\Phi_{p-m, p}[k]$ in (15).

The proposed four estimators only consider adjacent pilot blocks implied by $\Phi_{2i,2i+1}[k]$ in the non-reusing schemes and $\Phi_{i,i+1}[k]$ in the reusing schemes. Thus, the complexities of the proposed schemes are lower than the MLE.

- The MLE (16) neglects the issue of phase wrapping: the phase rotation between two pilot blocks with a separation of iQ is given as $\Delta\omega D\psi iQ$ and could grow beyond $\pm 2\pi$ when i is large, known as phase wrapping. In this aspect, the proposed estimators are more resilient against phase wrapping, since only adjacent pilot blocks are used.

Therefore, the proposed estimators are the low-complexity versions of the MLE in [38] and is more robust against phase wrapping. Estimation performance with phase wrapping is discussed in Section V-C. ■

Given $\widehat{\Delta\omega}$, the CPE θ is estimated by cross-correlating the pilot symbols with the received signal after CFO compensation, given as³

$$\hat{\theta} = -\angle \left[\sum_{i=0}^{\overline{N}_p} \sum_{q=0}^{M-1} e^{j\widehat{\Delta\omega}\psi D(iQ+q+L')} Y[iQ+q+L'] \times X^*[iQ+q] \right], \quad (17)$$

where $\overline{N}_p = N_p$ for the non-reusing schemes and $\overline{N}_p = N'_p$ for the reusing schemes. Then, the phase of the received data $Y[k]$ in data block i is corrected as

$$\tilde{Y}[k] = Y[k] e^{j(\widehat{\Delta\omega}\psi Dk + \hat{\theta})}, \quad k = (i-1)Q + M + q + L', \quad 0 \leq q \leq N-1. \quad (18)$$

Finally, the phase-corrected symbols $\tilde{Y}[k]$ are processed by a Viterbi decoder, yielding the decoded symbols given as $\hat{X}[k]$.

V. PERFORMANCE ANALYSIS

We analyze the theoretical bias and MSE performances of the proposed estimators. Firstly, we present the results without phase wrapping. Secondly, we analyze the performance degradation with phase wrapping and propose a method to avoid phase wrapping. The loss of the TR focusing gain is studied as well.

A. Bias and MSE Performances Without Phase Wrapping

For simplicity of analysis, we make the assumptions as shown in Appendix A. The bias and MSE performances are given as

$$\begin{aligned} \text{Bias}(\widehat{\Delta\omega}) &= \mathbb{E} [\widehat{\Delta\omega} - \Delta\omega], \\ \text{MSE}(\widehat{\Delta\omega}) &= \mathbb{E} [(\widehat{\Delta\omega} - \Delta\omega)^2]. \end{aligned} \quad (19)$$

Theorem 1: The four proposed estimators in (14) are unbiased under the assumptions shown in Appendix A, i.e.,

$$\text{Bias}(\widehat{\Delta\omega}) = 0. \quad (20)$$

Assuming that AOM-NR and MOA-NR use $N_p = 2B$ pilot blocks, while AOM-R and MOA-R use $N'_p = B + 1$

pilot blocks, the MSEs are given as

$$\text{MSE}(\widehat{\Delta\omega}) = \begin{cases} F \left(\frac{1}{MB} \left[\sigma^2 + \frac{\sigma^4}{2} \right] \right), & \text{AOM-NR} \\ F \left(\frac{1}{M} \left[\sigma^2 + \frac{\sigma^4}{2} \right] \right) / B, & \text{MOA-NR} \\ F \left(\frac{1}{MB} \left[\frac{\sigma^2}{B} + \frac{\sigma^4}{2} \right] \right), & \text{AOM-R} \\ V(M, \sigma^2), & \text{MOA-R} \end{cases} \quad (21)$$

where

$$F(y) = \frac{\int_0^{\frac{\pi}{2}} \frac{2x^2}{\sqrt{2\pi y}} e^{-\frac{\tan^2(x)}{2y}} \frac{1}{\cos^2(x)} dx}{Q^2 \psi^2 D^2}, \quad (22)$$

$$V(x, y) = \frac{F(y)}{B} + \frac{2(B-1)}{B^2 Q^2 \psi^2 D^2} U(x, y), \quad (23)$$

$$\begin{aligned} U(x, y) &= \int_{u=-\infty}^{\infty} \int_{v=-\infty}^{\infty} \text{atan}(u) \text{atan}(v) \\ &\quad \times \frac{x}{2\pi \left(y + \frac{v^2}{2} \right) \sqrt{1 - \frac{1}{(2+y)^2}}} e^{-\frac{x(u^2+v^2 + \frac{2uv}{2+y})}{y + \frac{v^2}{2}}} \frac{1}{2 \left(1 - \frac{1}{(2+y)^2} \right)} dudv. \end{aligned} \quad (24)$$

Proof: Proofs are given in Appendix B-A, B-B, B-C, and B-D. ■

Remark 2: For a fair comparison between the non-reusing and reusing schemes, we use different numbers of pilot blocks such that both schemes could formulate the same number of $\Phi_{i,i+1}[k]$ terms. For instance, in the AOM-R method, with $N'_p = B + 1$ pilot blocks, we could obtain a total of B terms of $\Phi_{i,i+1}[k]$ with $i = 0, 1, \dots, B$. Similarly, in AOM-NR, with $N_p = 2B$ pilot blocks, we could also obtain in total of B terms of $\Phi_{2i,2i+1}[k]$ with $i = 0, 1, \dots, B$. ■

B. Bias and MSE Performances With Phase Wrapping

Results of Theorem 1 should be modified when phase wrapping occurs as follows:

Theorem 2: When phase wrapping occurs, the bias and MSE of the proposed estimators are given by

$$\text{Bias}(\widehat{\Delta\omega})|_{PW} = \pm \frac{2z\pi}{Q\psi D}, \quad z \in \mathbb{Z}^+, \quad (25)$$

$$\text{MSE}(\widehat{\Delta\omega})|_{PW} = \text{MSE}(\widehat{\Delta\omega}) + \frac{4z^2\pi^2}{Q^2\psi^2 D^2}, \quad z \in \mathbb{Z}^+. \quad (26)$$

Proof: Proofs are given in Appendix B-E. ■

C. Limitation on Q to Avoid Phase Wrapping

Eq. (22) and (23) show that the MSE improves when Q becomes larger. However, when Q exceeds a certain boundary, phase wrapping occurs and introduces bias, degrading the MSE performances as shown in Theorem 2. In this part, we discuss how to choose Q appropriately in system design to avoid phase wrapping.

First, consider the ideal case without noise, (12) reduces to

$$\Phi_{0,1}[k] = |S[k]|^2 e^{j\Delta\omega Q\psi D}, \quad (27)$$

³Since we mainly focus on the CFO estimator in this paper, performance analysis of the CPE estimator is omitted.

and thus $\Delta\omega = \frac{\angle\Phi_{0,1}[k]}{QD\psi}$. However, $\Delta\omega \pm \frac{2z\pi}{Q\psi D}, z \in \mathbb{Z}^+$ produce the same values of $\Phi_{0,1}[k]$, giving rise to uncertainties on $\Delta\omega$. Such uncertainty is known as the phase wrapping issue, and it leads to an additional and growing phase in the compensated symbols $\tilde{Y}[k]$ which deteriorates the decoding performance. To avoid this, we must ensure that $|\Delta\omega Q\psi D| < \pi$. In the presence of noise, the condition can be written as

$$Q < \frac{\lambda\pi}{|\Delta\omega|D\psi}, \quad (28)$$

where $\lambda \in (0, 1]$ is a scaling factor introduced for robustness. Therefore, one should choose a large Q to improve the MSE performance, but not beyond the limitation imposed by (28).⁴

Remark 3: The MLE (15) considers pilot blocks with different separations and the maximum phase rotation between symbols inside two pilot blocks with B pilot blocks is $\Delta\omega D\psi B$. Therefore, the estimation range of $\Delta\omega$ to avoid phase wrapping shrinks by a factor of B in comparison with the proposed schemes. ■

D. Effect of $\Delta\omega$ on Channel Probing

In this part, we study the impact of $\Delta\omega$ on CP phase. As can be seen from (10), the effect of CFO is twofold: (i) it introduces an attenuation on the maximal TR focusing gain (ii) it leads to an additional phase rotation on the estimated CIR.

Firstly, we study how $\Delta\omega$ attenuates the TR focusing gain. Assume that the CIR is random and follows a certain distribution, and define the ratio between the expectation of $|\beta(\Delta\omega)|^2$ over the expectation of $|\beta(0)|^2$ in (11) as $\rho(\Delta\omega)$, shown as

$$\rho(\Delta\omega) = \frac{\mathbb{E} \left[\left| \sum_{\ell=0}^{L-1} |h[\ell]|^2 e^{-j\Delta\omega\psi\ell} \right|^2 \right]}{\mathbb{E} \left[\left(\sum_{\ell=0}^{L-1} |h[\ell]|^2 \right)^2 \right]}. \quad (29)$$

$\rho(\Delta\omega)$ provides insights on how $\Delta\omega$ affects the TR focusing gain. $\rho(\Delta\omega)$ under exponential decaying channel and complex Gaussian channel can be derived straightforwardly.

For exponential decaying channel, $\mathbb{E} [|h[\ell]|^2] = e^{-\frac{\ell T_s}{\sigma_T}}$, $\ell = 0, 1, \dots, L-1$, where σ_T is the delay spread of the channel. For complex Gaussian channel, $\mathbb{E} [|h[\ell]|^2] = \sigma_h^2$, $\ell = 0, 1, \dots, L-1$. The results are presented in the following theorem.

Theorem 3: $\rho(\Delta\omega)$ for the exponential decaying channel is

$$\rho(\Delta\omega) = \frac{1 - e^{-\frac{2LT_s}{\sigma_T}} + 1 - 2e^{-\frac{T_s L}{\sigma_T}} \cos(\Delta\omega\psi L) + e^{-\frac{2T_s L}{\sigma_T}}}{1 - e^{-\frac{2T_s}{\sigma_T}} + 1 - 2e^{-\frac{T_s}{\sigma_T}} \cos(\Delta\omega\psi) + e^{-\frac{2T_s}{\sigma_T}}}, \quad (30)$$

$$\frac{1 - e^{-\frac{2LT_s}{\sigma_T}}}{1 - e^{-\frac{2T_s}{\sigma_T}}} + \left(\frac{1 - e^{-\frac{LT_s}{\sigma_T}}}{1 - e^{-\frac{T_s}{\sigma_T}}} \right)^2$$

⁴Although $\Delta\omega$ is not known exactly, we could infer the range of $\Delta\omega$ based on the specifications of the local oscillators and use the maximum value of $\Delta\omega$, denoted as $\Delta\omega_{\max}$, to replace $\Delta\omega$ in (28).

TABLE I
PARAMETER SETTINGS IN SIMULATIONS

| Parameter | Notation | Value |
|-------------------------------|------------------------|---|
| Data Block Length | N | [256, 512, 1024, 2048] |
| Pilot Block Length | M | [16, 32, 64, 128] |
| # of Data Frames, Non-Reusing | $N_d = B$ | [13, 27, 55, 127] |
| # of Data Frames, Reusing | $N'_d = \frac{B+1}{2}$ | [7, 14, 28, 56] |
| Back-off Rate | D | [4, 8, 16] |
| Decimation Ratio | ψ | 4 |
| Channel Model | $h[\ell]$ | UWB, Bandwidth 125 MHz, $L = 30$, normalized |
| Chip-level NCFO | $\Delta\omega$ | 8×10^{-5} |
| Baseband Sampling Frequency | f_b | 125 MHz |
| Baseband Sampling Interval | T_b | 8 ns |
| Carrier Frequency | f_c | 5.8 GHz |
| Number of Iterations | I | 1×10^4 |

and $\rho(\Delta\omega)$ for complex Gaussian channel is

$$\rho(\Delta\omega) = \frac{L + \frac{1 - \cos(\Delta\omega\psi L)}{1 - \cos(\Delta\omega\psi)}}{L + L^2}. \quad (31)$$

Proof: Proofs are given in Appendix C. ■

Secondly, we discuss the phase rotation on CIRs caused by CFO. As shown by (10), the phase rotation associated with the ℓ -th channel tap is given as $\Delta\omega\psi\ell$, and the maximum phase rotation is $\Delta\omega\psi(L-1)$. For a parameter setting of $L = 30$, $\Delta\omega = 8 \times 10^{-5}$, $\psi = 4$, the maximum phase rotation is 0.0067 radians or 2.4 degrees, which is very small and can be ignored.

Now, we can conclude that the CIR phase rotation is less important than the TR focusing gain attenuation. In Section VI, we demonstrate that the loss of TR focusing gain is negligible as well. In summary, the CFO would only slightly affect the performance of TR communication.

VI. SIMULATION RESULTS

In this section, we present simulation results of the proposed CFO estimators and justify the theoretical analysis in Section V.

A. Parameter Settings

The parameters in simulations are summarized in Table I. We choose N_d and N'_d in the table for fair comparison between the reusing and non-reusing schemes as discussed in Remark 1 in Section V. Except otherwise mentioned, the experimental settings are given as (i) Perfect signature g is used at the AP. (ii) $\Delta\omega$ is static. (iii) Ultra-wideband (UWB) channel simulator in [39] is utilized. (iv) AOM-R method is used. (v) For all simulations, SNR is defined as $\text{SNR} = 1/\sigma^2$ ranging from 0 dB to 20 dB. (vi) Data blocks are modulated as QPSK while pilot blocks are modulated as BPSK.

In Fig. 4(a), we show the MSE performance versus SNR under different back-off rate D . For $D = 4$, we set $N = 1024$, $M = 32$, and $B = 14$. For $D = 8$ and $D = 16$, we scale N as $\frac{1024 \times 4}{D}$ and M as $\frac{32 \times 4}{D}$ for fairness, so that (i) the distance between two adjacent pilot blocks is fixed as $(M+N)D = 4224$ samples. (ii) The total number of data samples is fixed as $(M+N)DB + MDB = 59264$ samples. We observe that the performance degrades when D increases, which is expected based on (21) and (22). When $D = 4$, the MSE performances match well with the theoretical results in Theorem 1. However, when $D = 8$ and $D = 16$, the gap between the theoretical and

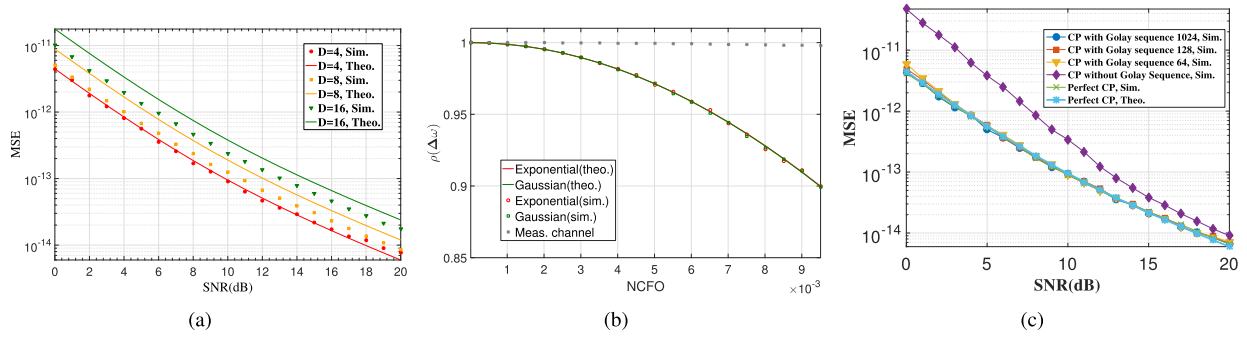


Fig. 4. (a) Effect of D on MSE, $N = \frac{1024 \times 4}{D}$, $M = \frac{32 \times 4}{D}$, $B = 14$, $D \in \{4, 8, 16\}$; (b) Effect of NCFO on $\rho(\Delta\omega)$ (c) Effect of NCFO on the CP phase, $N = 1024$, $M = 32$, $B = 14$, $D = 4$.

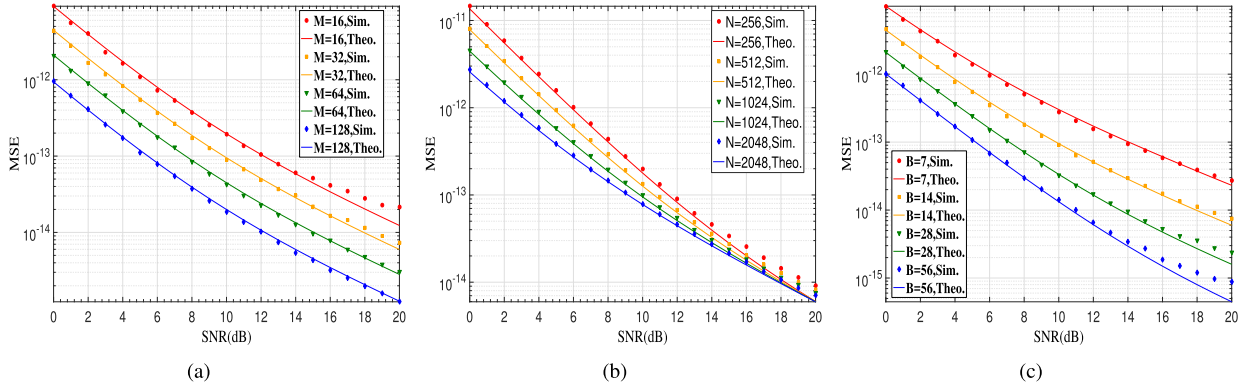


Fig. 5. (a) Effect of M on MSE, $N = 1024$, $M \in \{16, 32, 64, 128\}$, $B = 14$; (b) Effect of N on MSE, $(B, N) \in \{(56, 256), (28, 512), (14, 1024), (7, 2048)\}$, $M = 32$; (c) Effect of B on MSE, $N = 1024$, $M = 32$, $B \in \{7, 14, 28, 56\}$.

the simulation results enlarges. This can be justified by the fact that the length of a single pilot block is reduced by a factor of 2 and 4 for $D = 8$ and 16, and the Gaussian approximation is less accurate in (56), (61), (62), (63) in Appendix VIII-B, rendering the theoretical analysis less tenable. Despite the fact that a small D leads to better CFO estimations, it also results in an increased level of ISI and worsens the performance of data symbol decoding.

In Fig. 4(b), we demonstrate $\rho(\Delta\omega)$ in (29) under exponential decaying and complex Gaussian channel, as well as under a measured channel. The channel delay spread σ_T equals to $125T_s$ for exponential decaying channel [12]. $\Delta\omega$ varies from 1×10^{-5} to 1×10^{-2} . We observe that the simulation results match the theoretical results shown in Theorem 3. For the exponential decaying channel and the complex Gaussian channel, $\rho(\Delta\omega)$ drops to 0.89 when $\Delta\omega = 1 \times 10^{-2}$. For the measured channel, $\rho(\Delta\omega)$ only reduces slightly, indicating that the loss of TR focusing gain is negligible in practice. In the measured CFOs in practice, $\Delta\omega$ is on the order of 10^{-5} . Thus, the effect of $\Delta\omega$ on the CP phase can be neglected.

In Fig. 4(c), we show the MSE performance under perfect CP phase and imperfect CP phase with distorted signature. For the imperfect CP phase simulation, CFO is added to the randomly generated CIRs and thus distorts the signature $g[k]$. Also, we emulate the procedure of channel probing by transmitting a Golay sequence with $L_{GS} \in \{1024, 128, 32\}$ respectively for channel estimation. Moreover, we emulate the worst-case scenario without using Golay sequence. As can be seen from Fig. 4(c), the performances between perfect and imperfect signature $g[k]$ in presence of $\Delta\omega$ are almost

identical for different L_{GS} . Also, we find that it is necessary to use the Golay sequence for channel estimation. Combining with Fig. 4(b), we conclude that the effect of CFO in the CP phase can be ignored when the Golay sequence is utilized.

The effects of the parameters (M , N , B) on the MSE performances are shown in Fig. 5(a), Fig. 5(b), and Fig. 5(c) respectively. It can be seen that the theoretical results match well with the simulation results for all cases. The MSE performances improve when M , N , and B increases.

In Fig. 6(a) and Fig. 6(b), we compare the performance of MOA and AOM with and without reusing. We can see that the theoretical MSE agrees with the simulations, except when $N = 2048$ with $\text{SNR} \leq 6$ dB. However, the difference between AOM and MOA is negligible for both reusing and non-reusing cases. In Fig. 6(c), we compare AOM-R with AOM-NR, as well as MOA-R with MOA-NR under $N = 1024$. Clearly, reusing significantly enhances the performances.

Fig. 7(a) shows the performance of AOM-R estimator under different N , B , and $\Delta\omega$. The performance with $\Delta\omega = 5 \times 10^{-5}$ is identical to $\Delta\omega = 8 \times 10^{-5}$ for all (N, B) . However, the estimator fails when $(N, B) = (2048, 7)$ and $\Delta\omega = 1 \times 10^{-4}$, because the condition in (28) for phase wrapping avoidance is violated. According to (28), the largest tolerable $\Delta\omega$ is calculated by $|\Delta\omega_{\max}| = \frac{\pi}{Q\psi D} = 9.44 \times 10^{-5}$ with $N = 2048$, $M = 32$, $Q = M + N = 2080$, and $\lambda = 1$. Since $1 \times 10^{-4} > |\Delta\omega_{\max}|$, the estimator cannot produce reliable estimations. We also plot the MSE performance with phase wrapping when $N = 2048$ by setting $z = 1$ in (26). The theoretical performance with phase wrapping agrees with the simulation result.

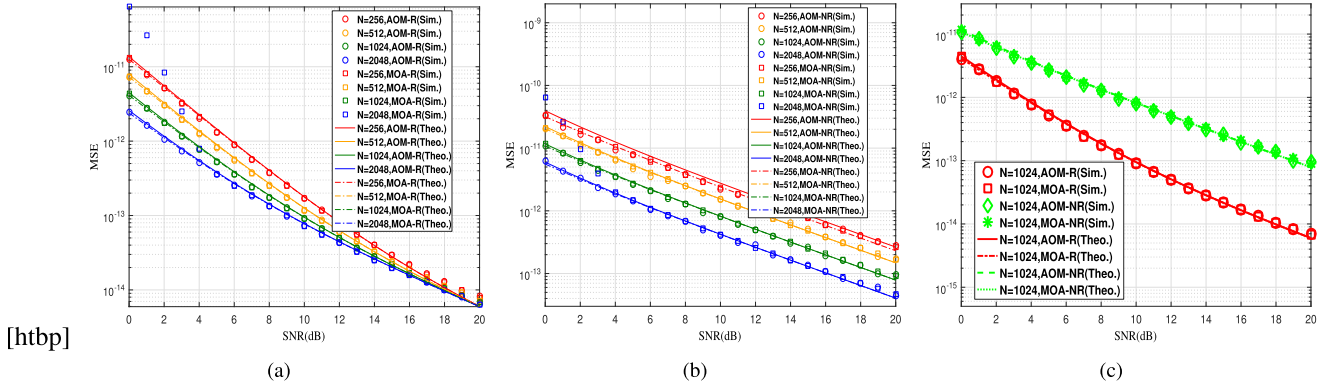


Fig. 6. Comparison between AOM and MOA: (a) reusing (b) non-reusing (c) $N = 1024$, $M = 32$, $B = 14$ for reusing and $B = 27$ for non-reusing.

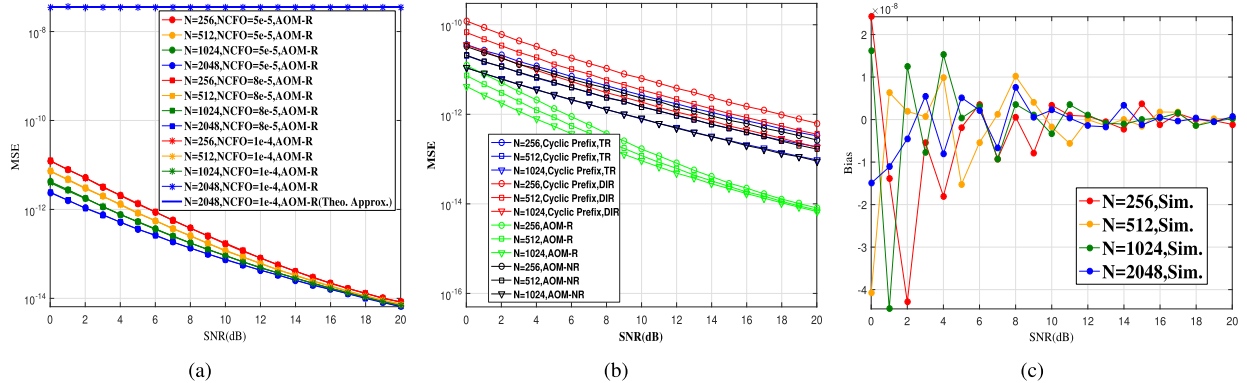


Fig. 7. (a) MSE performances under different $\Delta\omega$, $N \in \{256, 512, 1024, 2048\}$, $M = 32$, $B \in \{128, 56, 28, 14\}$, $\Delta\omega \in [5 \times 10^{-5}, 8 \times 10^{-5}, 1 \times 10^{-4}]$; (b) Comparison between the cyclic prefix scheme and the proposed schemes (c) Bias of estimation.

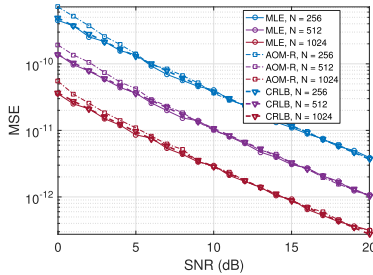


Fig. 8. Performance comparison among MLE, AOM-R, and CRLB.

In Fig. 7(b), we compare the performances between the conventional cyclic prefix based methods and the proposed methods. For the cyclic prefix method, the last M data symbols of each data block are appended before the start of the data block. The length of each data block is thus $Q = N + M$. The cyclic prefix schemes are simulated using TR transmission as well as direct transmission (DIR) without using the TR waveform. Using TR, the non-reusing schemes are identical with the cyclic prefix scheme when $N = 512$ or 1024 , and non-reusing scheme performs slightly better when $N = 256$. Schemes with reusing significantly outperform the cyclic prefix schemes. Performances of cyclic prefix schemes under DIR are worse than those with TR, which could be justified by the fact that the TR focusing gain in (11) enhances the performance of the estimator.

Fig. 7(c) shows the simulation results of bias for AOM-R under different N . The biases are negligible for all cases in comparison with a relatively large $\Delta\omega = 8 \times 10^{-5}$. Under the

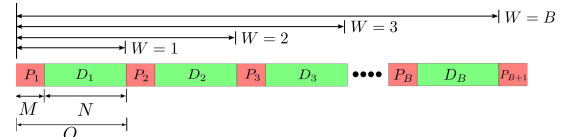


Fig. 9. Frame structure in experiments.

worst case of SNR = 0 dB, the maximum bias is -4.1×10^{-8} . Increasing N reduces the fluctuation of estimation. The bias vanishes gradually when SNR increases.

Fig. 8 compares the MSE performance of MLE and CRLB shown in [38] with the AOM-R scheme with $N \in \{256, 512, 1024\}$. We observe that the differences between MLE, AOM-R, and CRLB are negligible, illustrating the effectiveness of the proposed scheme.

VII. EXPERIMENT RESULTS

To evaluate the performance of the proposed CFO methods in practice, we use the TR prototypes as described in [30]. First, we perform over-the-cable (OTC) tests by connecting the transmitter and receiver via a cable with 50 dB attenuation. The transmission gain is 24 dB. Then, we perform over-the-air (OTA) tests using antennas with 27 dB transmission gain. The parameters for OTC and OTA are summarized into Table II.

Despite the fact that we use fixed Q and B for experiments, we could emulate the effects of different Q and B by concatenating adjacent transmission blocks together. This is illustrated in Fig. 9. By tuning the combining factor W , we could achieve

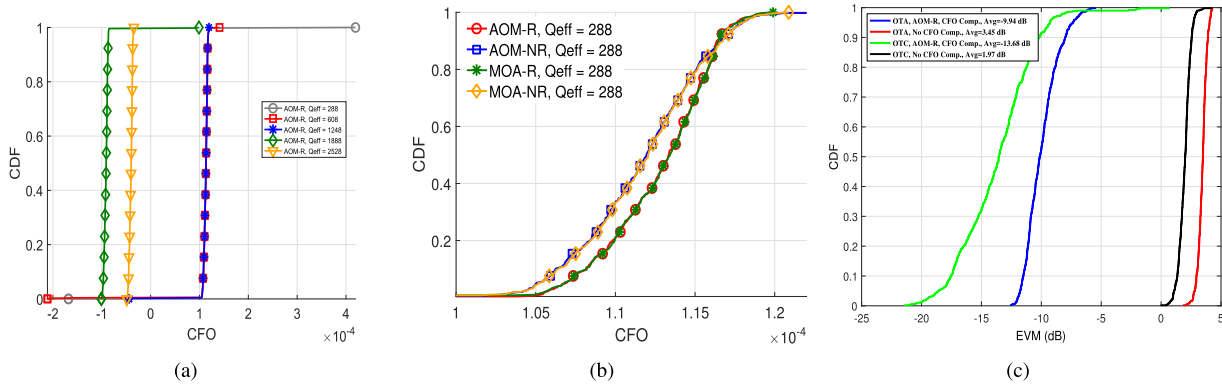


Fig. 10. (a) CDF of the estimated CFO using the AOM-R estimator, OTA. (b) CDF of the estimated CFO with and without reusing, OTA. (c) Effect of CFO compensation on EVM.

| W | Q_{eff} | M | B_{eff} | EVM, AOM-R (dB) | EVM, AOM-NR (dB) | $\Delta(\text{AOM})$ (dB) | EVM, MOA-R (dB) | EVM, MOA-NR (dB) | $\Delta(\text{MOA})$ (dB) |
|-----|------------------|-----|------------------|-----------------|------------------|---------------------------|-----------------|------------------|---------------------------|
| 2 | 288 | 32 | 39 | -9.94 | -9.72 | 0.22 | -9.96 | -9.74 | 0.22 |
| 4 | 608 | 32 | 19 | -9.95 | -9.56 | 0.39 | -9.97 | -9.59 | 0.38 |
| 8 | 1248 | 32 | 9 | -9.95 | -9.89 | 0.06 | -9.97 | -9.92 | 0.05 |

Fig. 11. Performance with scaling B_{eff} , OTA.

| W | Q_{eff} | M | B_{eff} | EVM, AOM-R (dB) | EVM, AOM-NR (dB) | $\Delta(\text{AOM})$ (dB) | EVM, MOA-R (dB) | EVM, MOA-NR (dB) | $\Delta(\text{MOA})$ (dB) |
|-----|------------------|-----|------------------|-----------------|------------------|---------------------------|-----------------|------------------|---------------------------|
| 2 | 288 | 32 | 39 | -13.68 | -13.31 | 0.37 | -13.72 | -13.35 | 0.37 |
| 4 | 608 | 32 | 19 | -13.70 | -13.25 | 0.45 | -13.72 | -13.27 | 0.45 |
| 8 | 1248 | 32 | 9 | -13.71 | -13.66 | 0.05 | -13.72 | -13.68 | 0.04 |

Fig. 12. Performance with scaling B_{eff} , OTC.

TABLE II
CONFIGURATION OF PARAMETERS IN EXPERIMENTS

| Parameter | Notation | Value |
|-----------------------------|----------|------------------|
| Data Block Length | N | 128 |
| Pilot Block Length | M | 32 |
| Transmission Block Length | Q | 160 |
| # of Frames | B | 88 |
| Back-off Rate | D | 4 |
| Decimation Ratio | ψ | 4 |
| Baseband Sampling Frequency | f_b | 125 MHz |
| Baseband Sampling Interval | T_b | 8 ns |
| Carrier Frequency | f_c | 5.8 GHz |
| Combining Factor | W | [2, 4, 6, 8, 16] |
| # of Trials | U | 500 |

different effective Q values, given by

$$Q_{\text{eff}}(W) = WN + (W - 1)M. \quad (32)$$

Given that the total length of data is calculated as $N \times B$, by choosing different W and thus different Q_{eff} , we should tune the effective number of data blocks as well, which takes the form as

$$B_{\text{eff}}(W) = \left\lfloor \frac{NB}{WN + (W - 1)M} \right\rfloor, \quad (33)$$

and $B_{\text{eff}}(W)$ is further rounded into the nearest odd number. For instance, when $W = 4$, we have $Q_{\text{eff}} = 608$ and $B_{\text{eff}} = 18$. Such flexibility enables us to obtain performances using different pilot separations with the same experimental results.

In practice, it is very hard to obtain the ground-truth CFO value. Therefore, to compare different schemes, we turn to the error vector magnitude (EVM) shown as

$$\text{EVM}[\hat{\mathbf{X}}] = 10 \log_{10} \frac{\|\hat{\mathbf{X}} - \mathbf{X}\|_2^2}{\|\mathbf{X}\|_2^2}, \quad (34)$$

where S is the total number of data symbols, $\hat{\mathbf{X}}$ is the vectorized decoded data symbols as shown in Section IV, and \mathbf{X} the transmitted symbols. EVM measures the average error energy of the received symbols in comparison with the ground-truth transmitted symbols and can indicate the overall system performance before and after CFO compensation.

A. Performance of Over-the-Air Test

In Fig. 10(a), we demonstrate the cumulative density functions (CDFs) of the estimated CFO using AOM-R scheme in one of the OTA tests. $Q_{\text{eff}} \in [288, 608, 1248, 1888, 2528]$, and $M = 32$. B_{eff} scales with Q_{eff} accordingly. Again, for fairness, we only use the first $\frac{B_{\text{eff}}+1}{2}$ pilot blocks for reusing schemes, and all B_{eff} pilot blocks for non-reusing cases. We observe that, for $Q_{\text{eff}} = 1888, 2528$, the estimated CFO is significantly different from the results of $Q_{\text{eff}} = 288, 608, 1248$. This could be due to that the condition for phase wrapping avoidance in (28) is violated when $Q_{\text{eff}} = 1888, 2528$. By investigating the EVM performances, we find that the CFO estimations under $Q_{\text{eff}} \in [288, 608, 1248]$ are the most accurate.

Fig. 10(b) illustrates the CDFs of the proposed four estimator with $Q_{\text{eff}} = 288$. As we can see, the CDF values corresponding to the reusing schemes are more concentrated, indicating that the estimations are more stable than the non-reusing schemes.

In Fig. 10(c), we draw the EVM CDFs before and after CFO compensation, with $Q_{\text{eff}} = 288$. We conclude that CFO compensation is necessary as it improves the EVM performance from 3.45 dB to -9.93 dB for OTA. We tabulate the averaged EVM into Table 11. The improvement of reusing against non-reusing is denoted by $\Delta(\text{AOM})$ and $\Delta(\text{MOA})$ respectively. The results imply that the improvement of increasing Q_{eff} could be balanced off by the decreasing of B_{eff} .

B. Performance of Over-the-Cable Test

The improvement of EVM after CFO compensation is shown in Fig. 10(c), and the results of EVM performances are summarized into Table 12. The EVM performances for OTC is much better than OTA since the ISI as well as the noise in cable transmission is smaller.

VIII. CONCLUSION

In this paper, we investigate the effect of CFO on TR systems and propose four schemes to estimate the small CFO inherent in wideband time-reversal systems with high accuracy. We derive the condition to avoid degradation caused by phase wrapping and study the impact of CFO on TR focusing gain. Bias and MSE performances of the four proposed estimators are theoretically analyzed and validated through simulations. Extensive experimental results validate the superiority and feasibility of the proposed estimators in a typical indoor environment.

APPENDIX A

ASSUMPTIONS IN DERIVATIONS

For simplicity, the noise term $n_{CP}[k]$ is rewritten as $n[k]$. The derivations in Appendix B-A, B-B, B-C, B-D follow the assumptions below:

Assumption 1: Phase wrapping does not occur.

Assumption 2: The data symbols $X[k]$ has a unit power.

Assumption 3: ISI is small enough to be neglected in $S[k]$, which holds with a large back-off rate D [12].

Assumption 4: $\Delta\omega$ is sufficiently small such that $|\beta(\Delta\omega)|^2 \approx 1$.

Assumption 5: $n[k]$ is zero-mean complex Gaussian random variable with equal power of $\sigma^2/2$ on its real and imaginary parts.

Assumption 6: $S[k]$ and $n[k]$ are uncorrelated with each other.

Assumption 7: The SNR is sufficiently large.

In Appendix B-E, we present the results when Assumption 1 does not hold, i.e., when phase wrapping occurs. Based on Assumption 2, 3, 4, the power of $S[k]$ is approximated as 1.

APPENDIX B

PERFORMANCE ANALYSIS OF THE PROPOSED ESTIMATORS

A. Performance Analysis of Angle-of-Mean, Non-Reusing

Here, we assume that the number of pilot blocks N_p is even.

1) *Case 1* ($N_p = 2$): Firstly, consider the case of $N_p = 2$. $\widehat{\Delta\omega}$ can be estimated by

$$\widehat{\Delta\omega} = \frac{\angle \left[\frac{1}{M} \sum_{k=0}^{M-1} \Phi_{0,1}[k] \right]}{QD\psi}, \quad (35)$$

where

$$\begin{aligned} & \sum_{k=0}^{M-1} \Phi_{0,1}[k] \\ &= \sum_{k=0}^{M-1} Y[k+L'] Y^*[k+Q+L'] \end{aligned}$$

$$\begin{aligned} &= \sum_{k=0}^{M-1} \left[S[k+L'] e^{-j(\Delta\omega D\psi(k+L')+\theta)} + n[k+L'] \right] \\ & \quad \left[S^*[k+Q+L'] e^{j(\Delta\omega D\psi(k+Q+L')+\theta)} + n^*[k+Q+L'] \right] \\ &= M e^{j\Delta\omega D\psi Q} + MA. \end{aligned} \quad (36)$$

Here, A is given as

$$\begin{aligned} A &= \frac{1}{M} \sum_{k=0}^{M-1} S[k+L'] n^*[k+Q+L'] e^{-j(\Delta\omega D\psi(k+L')+\theta)} \\ & \quad + S^*[k+Q+L'] n[k+L'] e^{j(\Delta\omega D\psi(k+Q+L')+\theta)} \\ & \quad + n^*[k+Q+L'] n[k+L']. \end{aligned} \quad (37)$$

Now, subtracting the ground-truth CFO $\Delta\omega$ on both sides of (35), we have

$$\begin{aligned} \widehat{\Delta\omega} - \Delta\omega &= \frac{\angle \left[1 + A e^{-j\Delta\omega D\psi Q} \right]}{QD\psi} = \frac{\text{atan} \left(\frac{\Im \left[1 + A e^{-j\Delta\omega D\psi Q} \right]}{\Re \left[1 + A e^{-j\Delta\omega D\psi Q} \right]} \right)}{QD\psi}. \end{aligned} \quad (38)$$

The expectation and variance of $\Re \left[1 + A e^{-j\Delta\omega D\psi Q} \right]$ can be computed as

$$\begin{aligned} \mathbb{E} \left[\Re \left[1 + A e^{-j\Delta\omega D\psi Q} \right] \right] &= 1, \\ \text{Var} \left[\Re \left[1 + A e^{-j\Delta\omega D\psi Q} \right] \right] &= \frac{1}{M} \left[\sigma^2 + \frac{\sigma^4}{2} \right], \end{aligned} \quad (39)$$

where the same results hold for $\Im \left[1 + A e^{-j\Delta\omega D\psi Q} \right]$. Further assume that

$$\mathbb{E} \left[\Re \left[1 + A e^{-j\Delta\omega D\psi Q} \right] \right] \gg \sqrt{\text{Var} \left[\Re \left[1 + A e^{-j\Delta\omega D\psi Q} \right] \right]}, \quad (40)$$

which is equivalent to

$$M \gg \sigma^2 + \frac{\sigma^4}{2}, \quad (41)$$

which is valid for large M under Assumption 7, since $\sigma^2 \ll 1$. Therefore, $\Re \left[1 + A e^{-j\Delta\omega D\psi Q} \right]$ can be approximated as a constant 1. Thus,

$$\text{atan} \frac{\Im \left[1 + A e^{-j\Delta\omega D\psi Q} \right]}{\Re \left[1 + A e^{-j\Delta\omega D\psi Q} \right]} \approx \text{atan} \left[\Im \left[1 + A e^{-j\Delta\omega D\psi Q} \right] \right]. \quad (42)$$

When M is sufficiently large, by virtue of law of large numbers, the distribution of $\Im \left[1 + A e^{-j\Delta\omega D\psi Q} \right]$ can be approximated by a Gaussian distribution described as

$$\Im \left[1 + A e^{-j\Delta\omega D\psi Q} \right] \sim \mathcal{N} \left(0, \frac{1}{M} \left[\sigma^2 + \frac{\sigma^4}{2} \right] \right). \quad (43)$$

For notational convenience, we denote $\frac{1}{M} \left[\sigma^2 + \frac{\sigma^4}{2} \right]$ as σ_x^2 , $\Im \left[1 + A e^{-j\Delta\omega D\psi Q} \right]$ as X where $X \sim \mathcal{N}(0, \sigma_x^2)$, and a random variable Y which is a function of X , given by $Y = \text{atan}(X)$. The probability density function (PDF) of Y can be calculated as

$$f_Y(y) = \frac{1}{\cos^2(y)} \frac{1}{\sqrt{2\pi\sigma_x^2}} e^{-\frac{\tan^2(y)}{2\sigma_x^2}}. \quad (44)$$

Therefore,

$$\mathbb{E}[Y] = \int_{-\frac{\pi}{2}}^{\frac{\pi}{2}} \frac{y}{\sqrt{2\pi\sigma_x^2}} e^{-\frac{\tan^2(y)}{2\sigma_x^2}} \frac{1}{\cos^2(y)} dy = 0, \quad (45)$$

$$\text{Var}[Y] = \mathbb{E}[Y^2] = \int_0^{\frac{\pi}{2}} \frac{2y^2}{\sqrt{2\pi\sigma_x^2}} e^{-\frac{\tan^2(y)}{2\sigma_x^2}} \frac{1}{\cos^2(y)} dy, \quad (46)$$

According to (38), we know that $QD\psi(\widehat{\Delta\omega} - \Delta\omega) = \angle[1 + Ae^{-j\Delta\omega D\psi Q}]$. Thus,

$$\mathbb{E}[QD\psi(\widehat{\Delta\omega} - \Delta\omega)] = 0 \quad (47)$$

indicates

$$\mathbb{E}[\widehat{\Delta\omega} - \Delta\omega] = \text{Bias}(\widehat{\Delta\omega}) = 0, \quad (48)$$

and

$$\begin{aligned} \text{Var}[QD\psi(\widehat{\Delta\omega} - \Delta\omega)] \\ = \int_0^{\frac{\pi}{2}} \frac{2y^2}{\sqrt{2\pi\sigma_x^2}} e^{-\frac{\tan^2(y)}{2\sigma_x^2}} \frac{1}{\cos^2(y)} dy \end{aligned} \quad (49)$$

indicates

$$\begin{aligned} \text{Var}[\widehat{\Delta\omega} - \Delta\omega] \\ = \text{MSE}(\widehat{\Delta\omega}) = \frac{\int_0^{\frac{\pi}{2}} \frac{2y^2}{\sqrt{2\pi\sigma_x^2}} e^{-\frac{\tan^2(y)}{2\sigma_x^2}} \frac{1}{\cos^2(y)} dy}{Q^2 D^2 \psi^2}, \end{aligned} \quad (50)$$

where $\sigma_x^2 = \frac{1}{M} [\sigma^2 + \frac{\sigma^4}{2}]$.

2) *Case II* ($N_p > 2$): Here, we generalize our results in Case I to more than two pilot blocks. Notice that $\widehat{\Delta\omega}_u$ and $\widehat{\Delta\omega}_v$ are uncorrelated if $u \neq v$. Following similar steps in Case I, we obtain

$$\begin{aligned} \text{Bias}(\widehat{\Delta\omega}) &= 0, \\ \text{MSE}(\widehat{\Delta\omega}) &= \frac{\int_0^{\frac{\pi}{2}} \frac{2y^2}{\sqrt{2\pi\sigma_x^2}} e^{-\frac{\tan^2(y)}{2\sigma_x^2}} \frac{1}{\cos^2(y)} dy}{Q^2 \psi^2 D^2} \end{aligned} \quad (51)$$

with $\sigma_x^2 = \frac{1}{M \frac{N_p}{2}} (\sigma^2 + \frac{\sigma^4}{2})$. By increasing the number of pilot blocks, σ_x^2 reduces linearly with N_p . Consequently, the estimator performance is improved. Setting $N_p = 2B$, we derive the MSE performance with AOM-NR in (21).

B. Performance Analysis of Angle-of-Mean, Reusing

First of all, we assume that the total number of pilot blocks N'_p is odd and $N'_p \geq 3$.

Now, we derive the performance when we reuse adjacent pilot blocks for estimation. In this case, $\widehat{\Delta\omega}_u$ and $\widehat{\Delta\omega}_v$ are correlated if $u \neq v, |u - v| = 1$ and uncorrelated otherwise.

Consider the case of $N'_p = 3$, where $\Delta\omega$ is estimated as

$$\widehat{\Delta\omega} = \frac{\angle \left[\frac{\sum_{k=0}^{M-1} \Phi_{0,1}[k] + \Phi_{1,2}[k]}{2M} \right]}{QD\psi}. \quad (52)$$

Subtracting the left hand side and the right hand side of (52) with $\Delta\omega$ yields

$$\begin{aligned} \widehat{\Delta\omega} - \Delta\omega \\ = \frac{\angle \left[1 + \frac{1}{2M} A' e^{-j\Delta\omega D\psi Q} + \frac{1}{2M} B' e^{-j\Delta\omega D\psi Q} \right]}{QD\psi} \end{aligned}$$

$$= \frac{\text{atan} \left[\frac{\Im \left[1 + \frac{1}{2M} A' e^{-j\Delta\omega D\psi Q} + \frac{1}{2M} B' e^{-j\Delta\omega D\psi Q} \right]}{\Re \left[1 + \frac{1}{2M} A' e^{-j\Delta\omega D\psi Q} + \frac{1}{2M} B' e^{-j\Delta\omega D\psi Q} \right]} \right]}{QD\psi}, \quad (53)$$

where

$$\begin{aligned} A' &= \sum_{k=0}^{M-1} S[k + L'] n^*[k + Q + L'] e^{-j(\Delta\omega D\psi(k+L')+\theta)} \\ &\quad + S^*[k + Q + L'] n[k + L'] e^{j(\Delta\omega D\psi(k+Q+L')+\theta)} \\ &\quad + n^*[k + Q + L'] n[k + L'] \end{aligned} \quad (54)$$

$$\begin{aligned} B' &= \sum_{k=0}^{M-1} S[k + Q + L'] n^*[k + 2Q + L'] e^{-j(\Delta\omega D\psi(k+Q+L')+\theta)} \\ &\quad + S^*[k + 2Q + L'] n[k + Q + L'] e^{j(\Delta\omega D\psi(k+2Q+L')+\theta)} \\ &\quad + n^*[k + 2Q + L'] n[k + Q + L']. \end{aligned} \quad (55)$$

After calculations, it can be shown that

$$\mathbb{E} \left[\Im \left[1 + \frac{1}{2M} A' e^{-j\Delta\omega D\psi Q} + \frac{1}{2M} B' e^{-j\Delta\omega D\psi Q} \right] \right] = 0. \quad (56)$$

Similarly, $\Im^2 \left[1 + \frac{1}{2M} A' e^{-j\Delta\omega D\psi Q} + \frac{1}{2M} B' e^{-j\Delta\omega D\psi Q} \right]$ can be written as

$$\frac{1}{4M^2} \sum_{k=0}^{M-1} [R[k] + O[k]]. \quad (57)$$

where $R[k] = \Im^2 [A' e^{-j\Delta\omega D\psi Q} + B' e^{-j\Delta\omega D\psi Q}]$, and $O[k]$ contains all other cross terms at time index k . The expectation of term $R[k]$ can be computed as

$$\mathbb{E} \left[\sum_{k=0}^{M-1} R[k] \right] = 2M\sigma^2 + M\sigma^4. \quad (58)$$

On the other hand, only *two terms* in $O[k]$ has non-zero mean, which are given as

$$\begin{aligned} O[k]_1 &= -\Re [S[k + L'] n^*[k + Q + L']] \\ &\quad \times \text{Re} [S^*[k + 2Q + L'] n[k + Q + L']] \sin^2 \\ &\quad \times (\Delta\omega D\psi(k + Q + L') + \theta), \\ O[k]_2 &= \Im [S[k + L'] n^*[k + Q + L']] \\ &\quad \times \Im [S^*[k + 2Q + L'] n[k + Q + L']] \cos^2 \\ &\quad \times (\Delta\omega D\psi(k + Q + L') + \theta). \end{aligned} \quad (59)$$

Thus

$$\mathbb{E} \left[\sum_{k=0}^{M-1} O[k] \right] = \mathbb{E} \left[\sum_{k=0}^{M-1} O[k]_1 + O[k]_2 \right] = -\frac{\sigma^2}{2}. \quad (60)$$

Finally

$$\begin{aligned} \mathbb{E} \left[\Im^2 \left[1 + \frac{1}{2M} A' e^{-j\Delta\omega D\psi Q} + \frac{1}{2M} B' e^{-j\Delta\omega D\psi Q} \right] \right] \\ = \frac{1}{2M} \left[\frac{\sigma^2}{2} + \frac{\sigma^4}{2} \right]. \end{aligned} \quad (61)$$

The derivations are similar for the real part, and we obtain

$$\mathbb{E} \left[\Re \left[1 + \frac{1}{2M} A' e^{-j\Delta\omega D\psi Q} + \frac{1}{2M} B' e^{-j\Delta\omega D\psi Q} \right] \right] = 1, \quad (62)$$

$$\mathbb{E} \left[\Re^2 \left[1 + \frac{1}{2M} A' e^{-j\Delta\omega D\psi Q} + \frac{1}{2M} B' e^{-j\Delta\omega D\psi Q} \right] \right] = \frac{1}{2M} \left[\frac{\sigma^2}{2} + \frac{\sigma^4}{2} \right]. \quad (63)$$

For sufficiently large M and N'_p and by virtue of law of large numbers, we could approximate both the real and imaginary part as Gaussian distributed random variable. Moreover, when

$$M \gg \frac{\sigma^2 + \sigma^4}{4}, \quad (64)$$

$\Re \left[1 + \frac{1}{2M} A' e^{-j\Delta\omega D\psi Q} + \frac{1}{2M} B' e^{-j\Delta\omega D\psi Q} \right]$ could be regarded as constant 1. Therefore,

$$\begin{aligned} \text{atan} \left[\frac{\Im \left[1 + \frac{1}{2M} A' e^{-j\Delta\omega D\psi Q} + \frac{1}{2M} B' e^{-j\Delta\omega D\psi Q} \right]}{\Re \left[1 + \frac{1}{2M} A' e^{-j\Delta\omega D\psi Q} + \frac{1}{2M} B' e^{-j\Delta\omega D\psi Q} \right]} \right] \\ \approx \text{atan} \left[\Im \left[1 + \frac{1}{2M} e^{-j\Delta\omega D\psi Q} (A' + B') \right] \right], \quad (65) \end{aligned}$$

and

$$\Im \left[1 + \frac{1}{2M} e^{-j\Delta\omega D\psi Q} (A' + B') \right] \sim \mathcal{N} \left(0, \frac{1}{2M} \left[\frac{\sigma^2}{2} + \frac{\sigma^4}{2} \right] \right). \quad (66)$$

We could derive the following:

$$\begin{aligned} \text{Bias}(\widehat{\Delta\omega}) = 0, \quad \text{MSE}(\widehat{\Delta\omega}) = \frac{\int_0^{\frac{\pi}{2}} \frac{2y^2}{\sqrt{2\pi\sigma_x^2}} e^{-\frac{\tan^2(y)}{2\sigma_x^2}} \frac{1}{\cos^2(y)} dy}{Q^2 \psi^2 D^2}, \\ \sigma_x^2 = \frac{1}{2M} \left[\frac{\sigma^2}{2} + \frac{\sigma^4}{2} \right]. \quad (67) \end{aligned}$$

Extending to N'_p pilot blocks, we have $\text{Bias}(\widehat{\Delta\omega}) = 0$ and $\text{MSE}(\widehat{\Delta\omega}) = F \left(\frac{1}{M(N'_p-1)} \left[\frac{\sigma^2}{N'_p-1} + \frac{\sigma^4}{2} \right] \right)$ with $F(y)$ given in (22). In comparison with the non-reusing case, if we set $N'_p = N_p + 1$, σ_x^2 is almost reduced by a factor of N_p . Consequently, the performance is significantly enhanced. Setting $N'_p = B + 1$, we derive the MSE performance with AOM-NR in (21).

C. Performance Analysis of Mean-of-Angle, Non-Reusing

Similar to Appendix B-A, we assume that the total number of pilot blocks N_p is even.

1) *Case I* ($N_p = 2$): For $N_p = 2$, MOA-NR reduces to AOM-NR. So, the results for MOA-NR are consistent with AOM-NR shown in (48) and (50).

2) *Case II* ($N_p > 2$): We rewrite the MOA-NR estimator in (14) as follows:

$$\begin{aligned} \widehat{\Delta\omega} = \frac{2}{N_p Q \psi D} \left[\angle \left[\frac{1}{M} \sum_{k=0}^{M-1} \Phi_{0,1}[k] \right] + \dots \right. \\ \left. + \angle \left[\frac{1}{M} \sum_{k=0}^{M-1} \Phi_{N_p-2, N_p-1}[k] \right] \right]. \quad (68) \end{aligned}$$

Each $\angle[\cdot]$ term in (68) is uncorrelated with any other term. The first and second order distributions of a single term in the form of $\angle \left[\frac{1}{M} \sum_{k=0}^{M-1} \Phi_{2i-2, 2i-1}[k] \right]$ are presented

in (48) and (50), respectively. (68) is simply the average of $\frac{N_p}{2}$ such terms. Therefore, we have

$$\begin{aligned} \text{Bias}(\widehat{\Delta\omega}) = 0, \quad \text{MSE}(\widehat{\Delta\omega}) = \frac{\int_0^{\frac{\pi}{2}} \frac{2y^2}{\sqrt{2\pi\sigma_x^2}} e^{-\frac{\tan^2(y)}{2\sigma_x^2}} \frac{1}{\cos^2(y)} dy}{\frac{N_p}{2} Q^2 \psi^2 D^2}, \\ \sigma_x^2 = \frac{1}{M} \left[\frac{\sigma^2}{2} + \frac{\sigma^4}{2} \right]. \quad (69) \end{aligned}$$

Setting $N_p = 2B$ leads to (21).

D. Performance Analysis of Mean-of-Angle, Reusing

Similar to Appendix B-B, assume that N'_p is odd. We need to consider the correlation between $\angle \left[\frac{1}{M} \sum_{k=0}^{M-1} \Phi_{i,i+1}[k] \right]$ and $\angle \left[\frac{1}{M} \sum_{k=0}^{M-1} \Phi_{i+1,i+2}[k] \right]$.

Without loss of generality, consider $i = 0$, and $N'_p = 3$. The estimator is given as

$$\widehat{\Delta\omega} = \frac{\angle \left[\frac{1}{M} \sum_{k=0}^{M-1} \Phi_{0,1}[k] \right] + \angle \left[\frac{1}{M} \sum_{k=0}^{M-1} \Phi_{1,2}[k] \right]}{2Q\psi D}. \quad (70)$$

Using the same trick in (37), (70) can be written as

$$\begin{aligned} \widehat{\Delta\omega} - \Delta\omega = \frac{1}{2Q\psi D} \left[\angle \left[1 + A e^{-j\Delta\omega D\psi Q} \right] \right. \\ \left. + \angle \left[1 + B e^{-j\Delta\omega D\psi Q} \right] \right], \quad (71) \end{aligned}$$

where

$$\begin{aligned} A = e^{j\Delta\omega D\psi Q} + \frac{1}{M} \sum_{k=0}^{M-1} S[k+L'] n^*[k+Q+L'] e^{-j(\Delta\omega D\psi(k+L')+\theta)} \\ + n[k+L'] S^*[k+Q+L'] e^{j(\Delta\omega D\psi(k+Q+L')+\theta)} \\ + n[k+L'] n^*[k+Q+L'], \quad (72) \end{aligned}$$

$$\begin{aligned} B = e^{j\Delta\omega D\psi Q} + \frac{1}{M} \sum_{k=0}^{M-1} S[k+Q+L'] n^*[k+2Q+L'] \\ \times e^{-j(\Delta\omega D\psi(k+Q+L')+\theta)} \\ + n[k+Q+L'] S^*[k+2Q+L'] e^{j(\Delta\omega D\psi(k+2Q+L')+\theta)} \\ + n[k+Q+L'] n^*[k+2Q+L']. \quad (73) \end{aligned}$$

It can be shown that

$$\mathbb{E} \left[\widehat{\Delta\omega} - \Delta\omega \right] = 0, \quad (74)$$

since

$$\mathbb{E} \left[\angle \left[1 + A e^{-j\Delta\omega D\psi Q} \right] \right] = \mathbb{E} \left[\angle \left[1 + B e^{-j\Delta\omega D\psi Q} \right] \right] = 0. \quad (75)$$

On the other hand, $\text{Var} \left[\widehat{\Delta\omega} - \Delta\omega \right]$ can be calculated as

$$\begin{aligned} \text{Var} \left[\widehat{\Delta\omega} - \Delta\omega \right] \\ = \frac{1}{4Q^2 D^2 \psi^2} \left\{ \mathbb{E} \left[\left(\angle \left[1 + A e^{-j\Delta\omega D\psi Q} \right] \right)^2 \right] \right. \\ \left. + \mathbb{E} \left[\left(\angle \left[1 + B e^{-j\Delta\omega D\psi Q} \right] \right)^2 \right] \right. \\ \left. + 2\mathbb{E} \left[\angle \left[1 + A e^{-j\Delta\omega D\psi Q} \right] \right. \right. \\ \left. \left. \angle \left[1 + B e^{-j\Delta\omega D\psi Q} \right] \right] \right\}, \quad (76) \end{aligned}$$

where

$$\begin{aligned} & \mathbb{E} \left[\left(\angle \left[1 + A e^{-j\Delta\omega D\psi Q} \right] \right)^2 \right] \\ &= \mathbb{E} \left[\left(\angle \left[1 + B e^{-j\Delta\omega D\psi Q} \right] \right)^2 \right] \\ &\approx \int_0^{\frac{\pi}{2}} \frac{2y^2}{\sqrt{2\pi\sigma_x^2}} e^{-\frac{\tan^2(y)}{2\sigma_x^2}} \frac{1}{\cos^2(y)} dy \end{aligned} \quad (77)$$

according to (46). Using (42), we have

$$\begin{aligned} & \angle \left[1 + A e^{-j\Delta\omega D\psi Q} \right] \angle \left[1 + B e^{-j\Delta\omega D\psi Q} \right] \\ &\approx \text{atan} \left[\Im \left(1 + A e^{-j\Delta\omega D\psi Q} \right) \right] \text{atan} \left[\Im \left(1 + B e^{-j\Delta\omega D\psi Q} \right) \right]. \end{aligned} \quad (78)$$

For convenience, we write $Y_1 = \Im \left(1 + A e^{-j\Delta\omega D\psi Q} \right)$ and $Y_2 = \Im \left(1 + B e^{-j\Delta\omega D\psi Q} \right)$, satisfying

$$Y_1 \sim \mathcal{N} \left(0, \frac{1}{M} \left[\sigma^2 + \frac{\sigma^4}{2} \right] \right), \quad Y_2 \sim \mathcal{N} \left(0, \frac{1}{M} \left[\sigma^2 + \frac{\sigma^4}{2} \right] \right), \quad (79)$$

We approximate the joint distribution of Y_1 and Y_2 as joint Gaussian distribution given as (80) as shown at the bottom of this page, where ρ is the correlation between Y_1 and Y_2 calculated as

$$\rho = \frac{\text{Cov}(Y_1, Y_2)}{\sqrt{\text{Var}(Y_1)\text{Var}(Y_2)}} = \frac{\mathbb{E}[Y_1 Y_2]}{\frac{1}{M} \left(\sigma^2 + \frac{\sigma^4}{2} \right)}, \quad (84)$$

After some calculations, we have

$$\rho = -\frac{1}{2 + \sigma^2}. \quad (85)$$

Substituting (85) into (80), we have (82), as shown at the bottom of this page, and finally

$$\begin{aligned} & \mathbb{E} \left[\text{atan} \left[\Im \left(1 + A e^{-j\Delta\omega D\psi Q} \right) \right] \text{atan} \left[\Im \left(1 + B e^{-j\Delta\omega D\psi Q} \right) \right] \right] \\ &= \int_{-\infty}^{+\infty} \int_{-\infty}^{+\infty} \text{atan}(y_1) \text{atan}(y_2) f_{Y_1, Y_2}(y_1, y_2) dy_1 dy_2. \end{aligned} \quad (86)$$

Thus, the MSE is given as (83), as shown at the bottom of this page. These results could be easily extended to $N'_p = B + 1 > 3$, which is shown in (21).

E. Performance Analysis With Phase Wrapping

The estimated CFO $\widehat{\Delta\omega}$ is related to the ground-truth CFO $\Delta\omega$ by

$$\widehat{\Delta\omega} = \Delta\omega + v \quad (87)$$

where v is the estimation noise.

From Theorem 1, we know that

$$\begin{aligned} \mathbb{E}[v] &= \mathbb{E}[\widehat{\Delta\omega} - \Delta\omega] = \text{Bias}(\widehat{\Delta\omega}) \\ \mathbb{E}[v^2] &= \mathbb{E}[(\widehat{\Delta\omega} - \Delta\omega)^2] = \text{MSE}(\widehat{\Delta\omega}). \end{aligned} \quad (88)$$

When phase wrapping occurs, the estimation $\widehat{\Delta\omega}$ in (87) should be modified into

$$\widehat{\Delta\omega} = \Delta\omega + v \pm \frac{2z\pi}{Q\psi D}, \quad z \in \mathbb{Z}^+, \quad (89)$$

Taking bias and MSE operations on (89) leads to (25) and (26).

APPENDIX C

ANALYSIS OF CFO EFFECT ON TR FOCUSING GAIN

F. Exponential Channel Profile

We could expand $\left(\sum_{\ell=0}^{L-1} |h[\ell]|^2 \right)^2$ as

$$\begin{aligned} \left(\sum_{\ell=0}^{L-1} |h[\ell]|^2 \right)^2 &= \sum_{\ell=0}^{L-1} |h[\ell]|^4 + \sum_{\ell_1=0}^{L-1} \sum_{\substack{\ell_2=0 \\ \ell_2 \neq \ell_1}}^{L-1} |h[\ell_1]|^2 |h[\ell_2]|^2. \end{aligned} \quad (90)$$

Similarly, $\left| \sum_{\ell=0}^{L-1} |h[\ell]|^2 e^{-j\psi \Delta\omega \ell} \right|^2$ can be written into

$$\begin{aligned} \left| \sum_{\ell=0}^{L-1} |h[\ell]|^2 e^{-j\psi \Delta\omega \ell} \right|^2 &= \sum_{\ell=0}^{L-1} |h[\ell]|^4 \\ &+ \sum_{\ell_1=0}^{L-1} \sum_{\substack{\ell_2=0 \\ \ell_2 \neq \ell_1}}^{L-1} |h[\ell_1]|^2 |h[\ell_2]|^2 e^{j\psi \Delta\omega (\ell_1 - \ell_2)}. \end{aligned} \quad (91)$$

$$f_{Y_1, Y_2}(y_1, y_2) = \frac{1}{2\pi \sigma_{Y_1} \sigma_{Y_2} \sqrt{1 - \rho^2}} e^{-\frac{1}{2(1-\rho^2)} \left[\frac{(y_1 - \mu_{Y_1})^2}{\sigma_{Y_1}^2} + \frac{(y_2 - \mu_{Y_2})^2}{\sigma_{Y_2}^2} - \frac{2\rho(y_1 - \mu_{Y_1})(y_2 - \mu_{Y_2})}{\sigma_{Y_1} \sigma_{Y_2}} \right]} \quad (80)$$

$$\mu_{Y_1} = \mu_{Y_2} \approx 0, \quad \sigma_{Y_1} = \sigma_{Y_2} \approx \sqrt{\frac{1}{M} \left[\sigma^2 + \frac{\sigma^4}{2} \right]} \quad (81)$$

$$f_{Y_1, Y_2}(y_1, y_2) = \frac{M}{2\pi \left(\sigma^2 + \frac{\sigma^4}{2} \right) \sqrt{1 - \frac{1}{(2+\sigma^2)^2}}} e^{-\frac{1}{2 \left(1 - \frac{1}{(2+\sigma^2)^2} \right)} \left[\frac{My_1^2}{\sigma^2 + \frac{\sigma^4}{2}} + \frac{My_2^2}{\sigma^2 + \frac{\sigma^4}{2}} + \frac{M^2 y_1 y_2}{2 + \sigma^2} \right]} \quad (82)$$

$$\begin{aligned} \text{MSE}(\widehat{\Delta\omega}) &= \frac{1}{4Q^2 \psi^2 D^2} \left[2 \int_0^{\frac{\pi}{2}} \frac{2y^2}{\sqrt{2\pi x}} e^{-\frac{\tan^2(y)}{2x}} \frac{1}{\cos^2(y)} dy \right. \\ &\quad \left. + 2 \int_{u=-\infty}^{\infty} \int_{v=-\infty}^{\infty} \text{atan}(u) \text{atan}(v) \frac{x}{2\pi \left(y + \frac{y^2}{2} \right) \sqrt{1 - \frac{1}{(2+y)^2}}} e^{-\frac{\left[\frac{x(u^2 + v^2 + \frac{2uv}{2+y})}{y + \frac{y^2}{2}} \right]}{2 \left(1 - \frac{1}{(2+y)^2} \right)}} dudv \right] \end{aligned} \quad (83)$$

$$\mathbb{E} \left[\sum_{\ell=0}^{L-1} |h[\ell]|^4 \right] = 2 \sum_{\ell=0}^{L-1} e^{-\frac{2\ell T_s}{\sigma_T}} = 2 \frac{1 - e^{-\frac{2LT_s}{\sigma_T}}}{1 - e^{-\frac{2T_s}{\sigma_T}}} \quad (92)$$

$$\mathbb{E} \left[\sum_{\substack{\ell_1=0 \\ \ell_2=0 \\ \ell_2 \neq \ell_1}}^{L-1} \sum_{\ell_2=0}^{L-1} |h[\ell_1]|^2 |h[\ell_2]|^2 \right] = \left(2 \frac{1 - e^{-\frac{2LT_s}{\sigma_T}}}{1 - e^{-\frac{2T_s}{\sigma_T}}} \right) - \left(\frac{1 - e^{-\frac{2LT_s}{\sigma_T}}}{1 - e^{-\frac{2T_s}{\sigma_T}}} \right) \quad (93)$$

$$\mathbb{E} \left[\sum_{\substack{\ell_1=0 \\ \ell_2=0 \\ \ell_2 \neq \ell_1}}^{L-1} \sum_{\ell_2=0}^{L-1} |h[\ell_1]|^2 |h[\ell_2]|^2 e^{j\psi \Delta\omega(\ell_1 - \ell_2)} \right] = \frac{1 - 2e^{-\frac{T_s L}{\sigma_T}} \cos(\psi \Delta\omega L) + e^{-\frac{2T_s L}{\sigma_T}}}{1 - 2e^{-\frac{T_s}{\sigma_T}} \cos(\psi \Delta\omega L) + e^{-\frac{2T_s}{\sigma_T}}} \quad (94)$$

Taking expectations, we can derive (92), (93), and (94) as shown at the top of this page. Finally, the TR focusing gain is calculated as (30).

G. Complex Gaussian Channel Profile

In this case, we can derive the following:

$$\mathbb{E} \left[\sum_{\ell=0}^{L-1} |h[\ell]|^4 \right] = 2L\sigma_h^4, \quad (95)$$

$$\mathbb{E} \left[\sum_{\substack{\ell_1=0 \\ \ell_2=0 \\ \ell_2 \neq \ell_1}}^{L-1} \sum_{\ell_2=0}^{L-1} |h[\ell_1]|^2 |h[\ell_2]|^2 \right] = L(L-1)\sigma_h^4, \quad (96)$$

$$\mathbb{E} \left[\sum_{\substack{\ell_1=0 \\ \ell_2=0 \\ \ell_2 \neq \ell_1}}^{L-1} \sum_{\ell_2=0}^{L-1} |h[\ell_1]|^2 |h[\ell_2]|^2 e^{j\psi \Delta\omega(\ell_1 - \ell_2)} \right] = \frac{2 - 2\cos(\psi \Delta\omega L)}{2 - 2\cos(\psi \Delta\omega)} \sigma_h^4 - L\sigma_h^4. \quad (97)$$

Therefore, we obtain (31).

REFERENCES

- [1] T.-D. Chiueh and P.-Y. Tsai, *OFDM Baseband Receiver Design for Wireless Communications*. Hoboken, NJ, USA: Wiley, 2007.
- [2] Y. P. E. Wang and T. Otosson, "Cell search in W-CDMA," *IEEE J. Sel. Areas Commun.*, vol. 18, no. 8, pp. 1470–1482, Aug. 2000.
- [3] T. Chulajata, H. M. Kwon, and K. Y. Min, "Coherent slot detection under frequency offset for W-CDMA," in *Proc. IEEE VTS 53rd Veh. Technol. Conf. (VTC Spring)*, vol. 3, May 2001, pp. 1719–1723.
- [4] M. Speth, S. A. Fechtel, G. Fock, and H. Meyr, "Optimum receiver design for wireless broad-band systems using OFDM. I," *IEEE Trans. Commun.*, vol. 47, no. 11, pp. 1668–1677, Nov. 1999.
- [5] P. Uolkosold, G. F. Tchere, S. Knedlik, and O. Loffeld, "Nonlinear least-squares frequency offset estimator and its simplified versions for flat-fading channels," in *Proc. Int. Symp. Commun. Inf. Technol. (ISCIT)*, Oct. 2006, pp. 246–249.
- [6] T. Keller and L. Hanzo, "Orthogonal frequency division multiplex synchronisation techniques for wireless local area networks," in *Proc. 7th IEEE Int. Symp. Pers., Indoor Mobile Radio Commun. (PIMRC)*, vol. 3, Oct. 1996, pp. 963–967.
- [7] J.-J. van de Beek, M. Sandell, and P. O. Borjesson, "ML estimation of time and frequency offset in OFDM systems," *IEEE Trans. Signal Process.*, vol. 45, no. 7, pp. 1800–1805, Jul. 1997.
- [8] T. M. Schmidl and D. C. Cox, "Robust frequency and timing synchronization for OFDM," *IEEE Trans. Commun.*, vol. 45, no. 12, pp. 1613–1621, Dec. 1997.
- [9] H. Minn, M. Zeng, and V. K. Bhargava, "On timing offset estimation for OFDM systems," *IEEE Commun. Lett.*, vol. 4, no. 7, pp. 242–244, Jul. 2000.
- [10] J. Kim, J. Noh, and K. Chang, "Robust timing frequency synchronization techniques for OFDM-FDMA systems," in *Proc. IEEE Workshop Signal Process. Syst. Design Implement.*, Nov. 2005, pp. 716–719.
- [11] Y. Chen *et al.*, "Time-reversal wireless paradigm for green Internet of Things: An overview," *IEEE Internet Things J.*, vol. 1, no. 1, pp. 81–98, Feb. 2014.
- [12] B. Wang, Y. Wu, F. Han, Y.-H. Yang, and K. J. R. Liu, "Green wireless communications: A time-reversal paradigm," *IEEE J. Sel. Areas Commun.*, vol. 29, no. 8, pp. 1698–1710, Sep. 2011.
- [13] F. Han, Y. H. Yang, B. Wang, Y. Wu, and K. J. R. Liu, "Time-reversal division multiple access over multi-path channels," *IEEE Trans. Commun.*, vol. 60, no. 7, pp. 1953–1965, Jul. 2012.
- [14] M. Speth, S. Fechtel, G. Fock, and H. Meyr, "Optimum receiver design for OFDM-based broadband transmission. II. A case study," *IEEE Trans. Commun.*, vol. 49, no. 4, pp. 571–578, Nov. 1999.
- [15] P. Pedrosa, R. Dinis, and F. Nunes, "Iterative frequency domain equalization and carrier synchronization for multi-resolution constellations," *IEEE Trans. Broadcast.*, vol. 56, no. 4, pp. 551–557, Dec. 2010.
- [16] Y. Chen, Y.-H. Yang, F. Han, and K. J. R. Liu, "Time-reversal wide-band communications," *IEEE Signal Process. Lett.*, vol. 20, no. 12, pp. 1219–1222, Dec. 2013.
- [17] C. Chen *et al.*, "Accurate sampling timing acquisition for baseband OFDM power-line communication in non-Gaussian noise," *IEEE Trans. Commun.*, vol. 61, no. 4, pp. 1608–1620, Apr. 2013.
- [18] M. Fink, "Acoustic time-reversal mirrors," in *Imaging of Complex Media With Acoustic and Seismic Waves (Topics in Applied Physics)*, vol. 84, M. Fink, W. Kuperman, J.-P. Montagner, and A. Tourin, Eds. Berlin, Germany: Springer, 2002.
- [19] B. Bogert, "Demonstration of delay distortion correction by time-reversal techniques," *IRE Trans. Commun. Syst.*, vol. 5, pp. 2–7, Dec. 1957.
- [20] F. Amoroso, "Optimum realizable transmitter waveforms for high-speed data transmission," *IEEE Trans. Commun. Technol.*, vol. COM-14, no. 1, pp. 8–13, Feb. 1966.
- [21] M. Fink, C. Prada, F. Wu, and D. Cassereau, "Self focusing in inhomogeneous media with time reversal acoustic mirrors," in *Proc. IEEE Ultrason. Symp.*, Oct. 1989, pp. 681–686.
- [22] C. Dorme, M. Fink, and C. Prada, "Focusing in transmit-receive mode through inhomogeneous media: The matched filter approach," in *Proc. IEEE Ultrason. Symp.*, vol. 1, Oct. 1992, pp. 629–634.
- [23] A. J. Devaney, "Time reversal imaging of obscured targets from multistatic data," *IEEE Trans. Antennas Propag.*, vol. 53, no. 5, pp. 1600–1610, May 2005.
- [24] D. Ciuonzo, G. Romano, and R. Solimene, "Performance analysis of time-reversal MUSIC," *IEEE Trans. Signal Process.*, vol. 63, no. 10, pp. 2650–2662, May 2015.
- [25] D. Ciuonzo and P. S. Rossi, "Noncolocated time-reversal MUSIC: High-SNR distribution of null spectrum," *IEEE Signal Process. Lett.*, vol. 24, no. 4, pp. 397–401, Apr. 2017.
- [26] J. M. F. Moura and Y. Jin, "Detection by time reversal: Single antenna," *IEEE Trans. Signal Process.*, vol. 55, no. 1, pp. 187–201, Jan. 2007.
- [27] Y. Jin and J. M. F. Moura, "Time-reversal detection using antenna arrays," *IEEE Trans. Signal Process.*, vol. 57, no. 4, pp. 1396–1414, Apr. 2009.
- [28] Y. Chen, B. Wang, Y. Han, H.-Q. Lai, Z. Safar, and K. J. R. Liu, "Why time reversal for future 5G wireless? [Perspectives]," *IEEE Signal Process. Mag.*, vol. 33, no. 2, pp. 17–26, Mar. 2016.
- [29] Y. Han, Y. Chen, B. Wang, and K. J. R. Liu, "Enabling heterogeneous connectivity in Internet of Things: A time-reversal approach," *IEEE Internet Things J.*, vol. 3, no. 6, pp. 1036–1047, Dec. 2016.

- [30] Z. H. Wu, Y. Han, Y. Chen, and K. J. R. Liu, "A time-reversal paradigm for indoor positioning system," *IEEE Trans. Veh. Technol.*, vol. 64, no. 4, pp. 1331–1339, Apr. 2015.
- [31] C. Chen, Y. Han, Y. Chen, and K. J. R. Liu, "Indoor global positioning system with centimeter accuracy using Wi-Fi [applications corner]," *IEEE Signal Process. Mag.*, vol. 33, no. 6, pp. 128–134, Nov. 2016.
- [32] Q. Xu, Y. Chen, B. Wang, and K. J. R. Liu, "Radio biometrics: Human recognition through a wall," *IEEE Trans. Inf. Forensics Security*, vol. 12, no. 5, pp. 1141–1155, May 2017.
- [33] Q. Xu, Y. Chen, B. Wang, and K. J. R. Liu, "TRIEDS: Wireless events detection through the wall," *IEEE Internet Things J.*, vol. 4, no. 3, pp. 723–735, Jun. 2017.
- [34] F. Zhang, C. Chen, B. Wang, H.-Q. Lai, and K. J. R. Liu, "A time-reversal spatial hardening effect for indoor speed estimation," in *Proc. IEEE Int. Conf. Acoust., Speech Signal Process. (ICASSP)*, Mar. 2017, pp. 5955–5959.
- [35] C. Chen *et al.*, "TR-BREATH: Time-reversal breathing rate estimation and detection," *IEEE Trans. Biomed. Eng.*, to be published.
- [36] M. Golay, "Complementary series," *IRE Trans. Inf. Theory*, vol. 7, no. 2, pp. 82–87, Apr. 1961.
- [37] B. M. Popovic, "Efficient Golay correlator," *Electron. Lett.*, vol. 35, no. 17, pp. 1427–1428, Aug. 1999.
- [38] M.-H. Cheng and C.-C. Chou, "Maximum-likelihood estimation of frequency and time offsets in OFDM systems with multiple sets of identical data," *IEEE Trans. Signal Process.*, vol. 54, no. 7, pp. 2848–2852, Jul. 2006.
- [39] A. F. Molisch *et al.*, "IEEE 802.15.4a channel model—Final report," in *Converging: Technology, Work and Learning*. Canberra, Australia: Australian Government Printing Service, 2004.



Chen Chen received the B.S. and M.S. degrees from the Department of Microelectronics, Fudan University, Shanghai, China, in 2010 and 2013, respectively. He is currently pursuing the Ph.D. degree with the Department of Electrical and Computer Engineering, University of Maryland, College Park, MD, USA. His research interests include biomedical signal processing, indoor localization, and wireless communications.

He was a recipient of multiple honors and awards, including the Excellent Graduate Student of Shanghai in 2013, the Distinguished Graduate Student Teaching Award and the Litton Industries Fellowship from the University of Maryland, in 2014 and 2015, respectively, and the Best Student Paper Award at the IEEE ICASSP 2016.



Yan Chen (SM'14) received the bachelor's degree from the University of Science and Technology of China in 2004, the M.Phil. degree from The Hong Kong University of Science and Technology in 2007, and the Ph.D. degree from the University of Maryland, College Park, MD, USA, in 2011. He was with Origin Wireless Inc. as a Founding Principal Technologist. Since 2015, he has been a Full Professor with the University of Electronic Science and Technology of China. His research interests include multimedia, signal processing, game theory, and wireless communications.

He was a recipient of multiple honors and awards, including the Best Student Paper Award at the IEEE ICASSP in 2016, the Best Paper Award at the IEEE GLOBECOM in 2013, the Future Faculty Fellowship and Distinguished Dissertation Fellowship Honorable Mention from the Department of Electrical and Computer Engineering in 2010 and 2011, the Finalist of the Dean's Doctoral Research Award from the A. James Clark School of Engineering, the University of Maryland in 2011, and the Chinese Government Award for outstanding students abroad in 2010.



Best Student Paper Award at the IEEE ICASSP in 2016.

Yi Han received the B.S. degree (Hons.) in electrical engineering from Zhejiang University, Hangzhou, China, in 2011, and the Ph.D. degree from the Department of Electrical and Computer Engineering, University of Maryland, College Park, MD, USA, in 2016. He is currently the Wireless Architect of Origin Wireless Inc. His research interests include wireless communication and signal processing.

Dr. Han was a recipient of the Class A Scholarship from Chu Kochen Honors College, Zhejiang University, in 2008. He was also a recipient of the



Hung-Quoc Lai (M'11) received the B.S. (*cum laude*), M.S., and Ph.D. degrees in electrical engineering from the University of Maryland, College Park, MD, USA, in 2004, 2006, and 2011, respectively. He is a Founding Member and currently is the Vice President of engineering at Origin Wireless Inc., which develops advanced time reversal wireless technologies for use in a wide variety of applications of indoor positioning/tracking, monitoring, security, radio human biometrics, wireless power transfer, and 5G communications.

Prior joining Origin Wireless Inc. in 2013, he was a Technical Lead in research and development of multiple-input multiple-output and cooperative communications at U.S. Army RDECOM CERDEC, Aberdeen Proving Ground, MD, USA. He is a Gates Millennium Scholar.



K. J. Ray Liu (F'03) was named a Distinguished Scholar-Teacher with the University of Maryland, College Park, MD, USA, in 2007, where he is the Christine Kim Eminent Professor of information technology. He leads the Maryland Signals and Information Group conducting research encompassing broad areas of information and communications technology with recent focus on smart radios for smart life.

He is a member of the IEEE Board of Director. He is a fellow of AAAS. He was the President of the

IEEE Signal Processing Society, where he has served as the Vice President - Publications and Board of Governor.

He was a recipient of the 2016 IEEE Leon K. Kirchmayer Technical Field Award on graduate teaching and mentoring, the IEEE Signal Processing Society 2014 Society Award, and the IEEE Signal Processing Society 2009 Technical Achievement Award. Recognized by Thomson Reuters as a Highly Cited Researcher.

He also received teaching and research recognitions from the University of Maryland, including university-level Invention of the Year Award; and college-level Poole and Kent Senior Faculty Teaching Award, Outstanding Faculty Research Award, and Outstanding Faculty Service Award, all from the A. James Clark School of Engineering. He has also served as the Editor-in-Chief of *IEEE Signal Processing Magazine*.